Advances in Water Resources 96 (2016) 323–338

Contents lists available at ScienceDirect

Advances in Water Resources

journal homepage: www.elsevier.com/locate/advwatres

A central-upwind scheme with artificial viscosity for shallow-water flows in channels

Gerardo Hernandez-Duenas[a,c,*], Abdelaziz Beljadid[b]

[a] Instituto de Matemáticas - Juriquilla, Universidad Nacional Autónoma de México, Blvd. Juriquilla 3001, Querétaro, 76230, México
[b] Massachusetts Institute of Technology, 77 Massachusetts Avenue, Cambridge, Massachusetts 02139, USA
[c] Investigación realizada gracias al Programa UNAM-DGAPA-PAPIIT IA103015

ARTICLE INFO

Article history:
Received 10 March 2016
Revised 4 July 2016
Accepted 30 July 2016
Available online 5 August 2016

Keywords:
Hyperbolic systems of conservation and balance laws
Semi-discrete central-upwind schemes
Shallow-Water equations
Channels with irregular geometry

ABSTRACT

We develop a new high-resolution, non-oscillatory semi-discrete central-upwind scheme with artificial viscosity for shallow-water flows in channels with arbitrary geometry and variable topography. The artificial viscosity, proposed as an alternative to nonlinear limiters, allows us to use high-resolution reconstructions at a low computational cost. The scheme recognizes steady states at rest when a delicate balance between the source terms and flux gradients occurs. This balance in irregular geometries is more complex than that taking place in channels with vertical walls. A suitable technique is applied by properly taking into account the effects induced by the geometry. Incorporating the contributions of the artificial viscosity and an appropriate time step restriction, the scheme preserves the positivity of the water's depth. A description of the proposed scheme, its main properties as well as the proofs of well-balance and the positivity of the scheme are provided. Our numerical experiments confirm stability, well-balance, positivity-preserving properties and high resolution of the proposed method. Comparisons of numerical solutions obtained with the proposed scheme and experimental data are conducted, showing a good agreement. This scheme can be applied to shallow-water flows in channels with complex geometry and variable bed topography.

1. Introduction

The shallow-water equations, also called Saint-Venant system model a large class of geophysical flows, characterized by their large length scale relative to their depth. The system consists of non-linear hyperbolic balance laws governed by conservation of mass and balance of momentum. The nonlinearity has important consequences, such as the generation of shock waves in finite time. Exact solutions are not available in general, and we need to rely on numerical approximations. An exception of this lies in a class of equilibrium solutions independent of time, arising when a delicate balance between source terms and flux gradients takes place. There are examples of geophysical flows in nature that are in fact, small perturbations to steady states. Although it is not within the scope of this paper, transoceanic tsunami propagation is one such situation (LeVeque et al., 2011). Equilibrium solutions can be computed exactly, to machine precision, and are used for reference when comparing to numerical solutions.

Numerical algorithms aimed at accurately computing shallow-water flows have been developed over the years. Different approaches achieving a number of desirable properties in the numerical schemes show the increasing interest in the community in the challenges hidden in this balance law. The treatment of jump discontinuities, near steady-state flows and the positivity of the water's depth is the focus of this study. Shock waves are usually correctly captured with the use of conservative schemes, which manage to carry out the conservation form of the law to the discrete level. When the initial data corresponds to an equilibrium state, one would expect that the numerical scheme recognizes such equilibrium. That does not always happen by itself unless we include a mechanism in the numerical algorithm to recognize all or a subclass of steady states. Schemes of that nature are called well balanced (Gosse and Leroux, 1996; Greenberg and Leroux, 1996). Simulations of small perturbations to steady states with schemes that are not well balanced can generate numerical errors of the same order of magnitude as the propagating perturbation. Well-balanced schemes have shown to be very accurate when computing near steady states. There are important geophysical flows that are not small perturbations to steady states, such as hydraulic jumps. See Figure 5.28 in Khan and Lai (2014). Even in such

* Corresponding author.
E-mail addresses: hernandez@im.unam.mx (G. Hernandez-Duenas), beljadid@mit.edu (A. Beljadid).

http://dx.doi.org/10.1016/j.advwatres.2016.07.021
0309-1708/

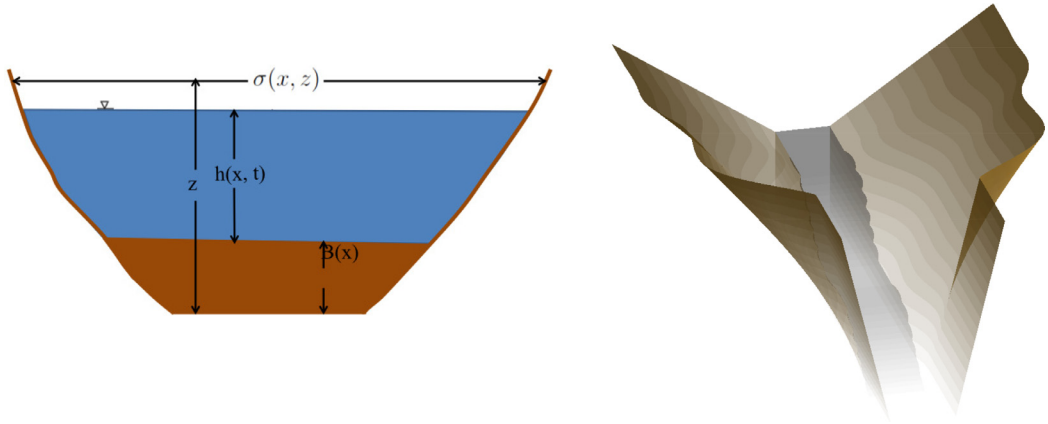

Fig. 1. Left: Schematic of channel with a description of the variables involved in the model. Right: Channel used in the dam break problem in Section 4.4.

situations, the well-balance property adds accuracy to the numerical approximations. Numerically maintaining the positivity of water's depth is another challenging task. Assuming that we start with positive values of water's depth in our flow, we would like to maintain that positivity as the flow evolves in time. This positivity-preserving property is desirable in any scheme treating near dry states (Audusse et al., 2004; Kurganov and Levy, 2002; Perthame and Simeoni, 2001).

As it is the case for other conservation and balance laws, Roe-type upwind schemes are popular and successful in shallow-water simulations. Upwind schemes developed in Roe (1987), are based on local linearizations of the flux Jacobian and its eigen-spectrum. They have shown to have a great performance near shock waves by capturing jump and contact discontinuities very accurately. Many numerical difficulties can be solved using upwind schemes by directly treating the waves' families in the local linearizations and their amplitudes. For instance, wave-propagation algorithms with Riemann problems at the center of each grid cell are used for near steady-state flows (LeVeque, 1998), where the flux difference at the center exactly cancels the source terms. Other approaches for near steady-state flows include capturing methods using interface values (Jin, 2001), hydrostatic reconstructions (Audusse et al., 2004), and WENO reconstructions (Noelle et al., 2006; 2007). An augmented Rieman solver that uses wave-propagation algorithms is described in George (2008). See also the book (Bouchut, 2004) and references therein. The Q-schemes introduced in Castro et al. (2001) were used in Castro et al. (2004) to solve two layer shallow-water systems. There are several other classes of schemes that have been used to solve the shallow-water equations. For instance, a kinetic scheme with an elegant and natural way of achieving the positivity-preserving property was derived in Perthame and Simeoni (2001).

Another category of successful schemes in a variety of balance laws is the class of central-upwind schemes, introduced in Kurganov et al. (2001), Kurganov and Tadmor (2000), and further developed in Kurganov and Lin (2007), Kurganov and Tadmor (2002). The central-upwind schemes are designed for balance laws in general, and are free of Riemann solvers. The schemes use, however, spectral information in the one-sided local speeds in the numerical flux. See Russo (2001), Vuković and Sopta (2003) and references therein. Central-upwind schemes achieving both the well-balance and the positivity-preserving property in shallow-water flows were presented in Kurganov and Levy (2002), Kurganov and Petrova (2007), Beljadid et al. (2016).

In open channel flows the component of the velocity vector parallel to the channel axis is dominant and the flow has relatively uniform distribution over the channel's cross sections. Thus, it is assumed that the parameters of the flow depend on the spatial coordinate along the channel axis and time (Szymkiewicz, 2010). The flow can be characterized using the cross-sectional wet area and averaged quantities such as the discharge, representing the mass of water flowing through cross-sections per unit time and the average flow velocity in each of these sections. This leads to a 1D model of shallow-water equations for flows through channels which has many applications in hydraulics for which several numerical schemes have been developed (Garcia-Navarro and Vazquez-Cendon, 2000; Khan and Lai, 2014; Russo, 2005; Szymkiewicz, 2010; Vázquez-Cendón, 1999). The governing equations can be written as a system of non-linear hyperbolic conservation laws. The corresponding shallow-water equations were first presented in Garcia-Navarro and Vazquez-Cendon (2000), Vázquez-Cendón (1999), and can actually be derived from the Euler equations by cross-sectional averaging under appropriate boundary conditions at the bottom topography, walls and surface (Hernández-Dueñas and Karni, 2011). The channel's geometry extends in one horizontal direction (x). At each location x of the channel, its width changes vertically according to an arbitrary function $\sigma(x, z)$ of height. See Fig. 1 for a complete description of the channel and variables. The bottom elevation, denoted by $B(x)$, varies along x and it is uniform in each cross section. The model is valid for flows traveling in the direction of the channel (x), and the zonal velocity at time t and location x is given by $u(x, t)$. The water's depth is denoted by $h(x, t)$, with total height $w = h + B$. The conserved variables are the cross-sectional wet area given by the vertical integral of the width from the bottom to the water's surface $A = \int_B^w \sigma(x, z)dz$, and the discharge $Q = Au$. Stationary (at rest) and other steady-state flows (in motion) arise when a delicate balance between the source terms and flux gradients occurs. The irregular geometry and the integration involved in the expression for the wet area calculation originates a richer family of equilibrium solutions than those compared to channels with vertical walls.

For many practical hydraulic applications, the use of 1D shallow water model is relevant. We need to choose a good compromise between the benefit of using 2D shallow water models, its complexity and accuracy of numerical methods and their simplicity in the case of 1D shallow water models. Shallow water flows in channels can be seen as one-dimensional flows with two-dimensional aspects when the geometry and topography are irregular. In this sense, the flows studied here can be considered as an intermediate case between the one- and two- dimensional flows. One advantage of this intermediate case is the availability of a rich variety of exact non-trivial steady state solutions. This is more difficult to analyze in two-dimensional flows. The variety of steady-state flows in the

intermediate case is much richer than the class of steady states that can be found in channels with vertical walls. Furthermore, the expression for the wet area involves an integral of the width from the bottom topography to the water's surface. As a consequence, the balance between the flux gradients and source terms in steady states becomes very delicate. This makes more difficult to satisfy the well-balance and positivity-preserving properties simultaneously. For all of the above reasons, we chose flows in channels to implement the artificial viscosity technique. The present setting is suitable for analyzing the viability of the new technique to adapt to systems where the conserved variables have more complicated expressions.

A well-balanced upwind scheme for channels with irregular geometries was derived in Hernández-Dueñas and Karni (2011). Although theoretically it does not formally preserve positivity, the entropy fix usually implemented in upwind schemes showed to be efficient in treating near-dry states. A central-upwind scheme for channels with vertical walls and horizontally varying width was considered in Balbás and Karni (2009), and it was based on the schemes in Kurganov and Levy (2002), Kurganov and Petrova (2009). The positivity-preserving property first achieved in Kurganov and Petrova (2007) was extended to channels in Balbás and Hernandez-Duenas (2014), where the flux and source terms involved integral terms. Such extension was not trivial since the integration involved in the expression for the flux and source terms is now more coupled together with the geometry and topography. Other central schemes for flows in channels are found in Črnjarić-Žic et al. (2004).

The central-upwind scheme proposed for shallow-water flows in channels in Balbás and Hernandez-Duenas (2014) is based on non-oscillatory second order reconstructions. The non-oscillatory reconstructions are made with the use of nonlinear limiters. See Harten (1983), Shu (2009), Sweby (1984) and references therein. Extending this technique to higher orders is difficult and computationally expensive when nonlinear limiters come into play. For instance, in Shu (2009) it was reported that higher order WENO schemes may be 3 to 10 times computationally more expensive, compared to the second order high resolution scheme. In Kurganov and Liu (2012), the use of an adaptive artificial viscosity is proposed as an alternative for hyperbolic systems of conservation laws and the special case of the shallow-water system is reproduced in detail in Chen et al. (2013). The artificial viscosity implementation consists of using diffusion coefficients that are very small in smooth regions according to the formal order of accuracy of the scheme, and it becomes strong enough near shock waves to avoid oscillations. This is done maintaining the consistency of the numerical discretization, and it is conservative by construction. The adaptive artificial viscosity is proposed as an alternative to keep high accuracy and resolution power at a low computational cost. In particular, it was reported in Kurganov and Liu (2012) that the scheme with artificial viscosity is 54.1% faster compared to a WENO5 reconstruction in the efficiency tests considered there.

In this paper, we extend the above approach to shallow-water flows along channels with non-uniform cross sections of arbitrary shape and bottom topography, as described above. Such extension is not trivial since the artificial viscosity interacts with the source terms, flux differences and conserved variables which now have integral forms dictated by the geometry and topography. In particular, the artificial viscosity coefficients need to be computed carefully so that they vanish for steady states at rest (see Eq. (21)), which ensures that the new artificial viscosity term in the numerical scheme does not interfere with the well-balance property. On the other hand, the CFL condition needs to be modified in a very special way to satisfy the positivity-preserving property, and the inequality that usually involves spectral information now also includes the artificial viscosity coefficients. See Proposition 1 for more details.

The paper is structured as follows. In Section 2 we provide a description of the system of shallow-water flows in channels, describe its main and basic properties while explaining the numerical challenges in each of them. In Section 3 we describe the numerical scheme, the desirable properties one can achieve with the algorithm, and the order of the steps we need to follow. We explain how it can be implemented to create a numerical scheme that satisfies the well-balance and positivity-preserving properties. Different numerical tests in Section 4 corroborate the merits of the scheme, including comparisons of our numerical results with real experimental data. Section 5 is devoted to the discussion of the main contributions of the paper. Finally, Section 6 provides some concluding remarks.

2. The model equations and properties

The shallow-water equations for flows through channels with variable cross-section are given by Garcia-Navarro and Vazquez-Cendon (2000), Hernández-Dueñas and Karni (2011),

$$\partial_t A + \partial_x Q = 0 \tag{1a}$$

$$\partial_t Q + \partial_x \left(Au^2 + p\right) = I - g\sigma_B h B', \tag{1b}$$

where h denotes the depth of the layer, u the cross-sectional velocity, $B(x)$ the bottom topography, $B' = \frac{dB}{dx}$, $\sigma(x, z)$ the width of the channel at a cross section x and height z, $A = \int_B^{B+h} \sigma(x, z)\, dz$ is the cross-sectional wet area, $Q = Au$ is the flow rate or discharge, $\sigma_B(x) = \sigma(x, B(x))$ denotes the channel's width at the bottom topography $z = B(x)$, and g the acceleration of gravity. The cross-sectional integrated hydrostatic pressure is given by

$$p = g \int_B^w (w - z)\sigma(x, z)\, dz, \tag{2}$$

where $w = h + B$ denotes the total water elevation. The cross-sectional averaged pressure-geometry variation $I(x, t)$ that appears as a source term is given by

$$I(x, t) = g \int_B^w (w - z)\sigma_x(x, z)\, dz. \tag{3}$$

We note that this source term involves x-derivatives of the geometry only, which does not alter the Rankine-Hugoniot conditions, assuming that σ is smooth with respect to x and z.

For reference to the standard 1D shallow-water equations, we provide in Table 1 the definitions and their more familiar value in the case of rectangular channels with no width variation $\sigma = 1$. The corresponding equations are

$$h_t + (hu)_x = 0 \tag{4a}$$

$$(hu)_t + \left(hu^2 + \frac{gh^2}{2}\right)_x = -ghB_x. \tag{4b}$$

2.1. Properties of the system

Hyperbolicity and many other properties of the system can be analyzed by writing it in quasilinear form $U_t + A(U)U_x = S$. A simple manipulation of the equations, valid for smooth flows, gives

$$\begin{pmatrix} A \\ Q \end{pmatrix}_t + \begin{pmatrix} 0 & 1 \\ c^2 - u^2 & 2u \end{pmatrix} \begin{pmatrix} A \\ Q \end{pmatrix}_x = \begin{pmatrix} 0 \\ c^2\left(h\sigma_{\text{var}}(x, t) - \sigma_B B'\right) \end{pmatrix}, \tag{5}$$

where $\sigma_{\text{var}}(x, t) = \frac{1}{h}\int_B^w \sigma_x(x, z)\, dz$ is the averaged width variation, $c = \sqrt{gA/\sigma_T}$ is the speed of sound, and $\sigma_T = \sigma(x, w)$ is the width of the channel at the water's surface. We note that c reduces to the familiar expression $c = \sqrt{gh}$ for rectangular channels.

Table 1
Variables' definitions.

Variable	Definition/Notation	Vertical walls
Channel's width	$\sigma(x, z)$	1
Bottom topography	$B(x)$	$B(x)$
Water's depth/Total height	$h(x,t), w = h + B$	$h(x,t), w = h + B$
Wet area	$A = \int_B^w \sigma(x,z)dz$	h
Velocity	$u(x, t)$	$u(x, t)$
Bottom channel's width	$\sigma_B(x) = \sigma(x, z = B(x))$	1
Surface channel's width	$\sigma_T(x,t) = \sigma(x, z = w(x,t))$	1
Speed of sound	$c = \sqrt{gA/\sigma_T}$	$c = \sqrt{gh}$
Cross-sectional averaged pressure	$p = g\int_B^w (w - z)\sigma(x,z)dz$	$\frac{gh^2}{2}$
Cross-sectional averaged pressure-geometry variation	$I = g\int_B^w (w - z)\sigma_x(x,z)dz$	0

The system (1) is hyperbolic, with eigenvectors and eigenvalues

$$R = \begin{pmatrix} 1 & 1 \\ u-c & u+c \end{pmatrix} \quad \Lambda = \begin{pmatrix} u-c & 0 \\ 0 & u+c \end{pmatrix}. \tag{6}$$

The system looses hyperbolicity in the so-called dry states with vanishing water's depth ($h = 0$). The shallow-water flows are characterized by the nondimensional Froude number $F = |u|/c$. Subcritical flows have Froude numbers less than one, which occurs when the flow speed does not exceed the speed of sound. Froude numbers larger than one define supercritical flows (Farmer and Armi, 1986).

Special solutions that can be computed exactly are those independent of time, or steady states. Such steady states occur due to a delicate balance between the flux gradients and the source terms, as described in the introduction. Simple manipulations of the equations, valid when the flow is smooth, characterize the steady states by two invariants. One of them is the flow rate Q, which accounts for the volume of fluid per unit time crossing at a given channel's cross section. The other invariant is E, the energy per unit of cross sectional area, and both quantities are given by

$$Q \equiv Au = Const, \quad E \equiv \frac{1}{2}u^2 + g(h + B) = Const, \tag{7}$$

among which it is easy to recognize the steady state of rest

$$u = 0, \quad h + B = Const. \tag{8}$$

Exact solutions for smooth steady-states can be found by solving

$$E = \frac{1}{2}\frac{Q^2}{A^2} + g(h + B), \tag{9}$$

for a given Q, E, $B(x)$, $\sigma(x, z)$. A rootfinding method easily gives us exact solutions to machine precision.

As it occurs in hyperbolic balance laws, discontinuities can form in finite time, giving rise to weak solutions. This can happen to equilibrium solutions as well. In such cases, it is easy to verify that the discharge is still constant. On the contrary, the energy is piecewise constant, changing across shock waves. These solutions for channels with (non-uniform) rectangular cross-sections are analyzed in Armi (1986), Armi and Farmer (1986), Farmer and Armi (1986).

3. The numerical central upwind scheme and details

Numerically computing the shallow-water system (1) poses a number of challenges. One consequence of the nonlinearity of the flux is the presence of shock waves that appear in finite time even if the initial conditions are smooth. Robust conservative numerical schemes are required to accurately compute discontinuous solutions. Equilibrium solutions arise when a delicate balance occurs between the flux gradients and the source terms. Some flows of interest are in fact small perturbations to such steady states. Numerical schemes that do not have those considerations in mind may produce numerical errors of the same order of magnitude as the evolving perturbations. A common strategy to avoid unaccepted numerical errors is to enable the scheme to recognize steady states at rest so that it remains constant in time in such flows. Numerical schemes that enjoy that property are called well-balanced methods, and such property has shown to be crucial in the computation of near steady state flows.

Dam-break and other problems involving near dry states is another challenge we include in this study. Numerical errors in near dry states may make the water's depth negative, which is not physically relevant or allowed. The system looses hyperbolicity and the numerical computation can fail. Positivity-preserving numerical schemes enjoy the property that if we start with positive values of h, the data maintains the positivity of it in subsequent steps. Numerical schemes with that property enhance stability near dry states.

In this section, we describe a central-upwind scheme to accurately compute shallow-water flows in channels as modelled by (1). In our numerical approach we take into consideration the well-balance and positivity-preserving properties. The approach here is different from existing schemes for shallow-water flows in channels as it avoids the use of nonlinear limiters and instead constructs an artificial viscosity to be negligible in smooth regions and strong enough near shock waves to control oscillations near jumps. The scheme extends the works in Chen et al. (2013), Kurganov and Liu (2012) where artificial viscosity is used for shallow-water flows (not in channels). Here we consider a shallow-water system in channels with irregular geometries, not necessarily rectangular, inducing more strongly coupled steady states with the geometry and topography. The use of artificial viscosity introduces one more element interplaying with the rest of the properties. The implementation of artificial viscosity instead of the nonlinear limiters allows us to consider higher order numerical schemes at a low computational expense.

3.1. The semi-discrete form of the proposed central-upwind scheme with artificial viscosity

The description of the proposed scheme can be done for balance laws in general. We write our system (1) in the general form

$$\mathbf{v}_t + \mathbf{f}(\mathbf{v})_x = \mathbf{S}(\mathbf{v}, x), \tag{10}$$

with

$$\mathbf{v} = \begin{pmatrix} A \\ Q \end{pmatrix}, \quad \mathbf{f}(\mathbf{v}) = \begin{pmatrix} Q \\ Au^2 + p \end{pmatrix}, \tag{11}$$

on the left hand side, and a source term given by

$$\mathbf{S} = \begin{pmatrix} 0 \\ I - g\sigma_B hB' \end{pmatrix}. \tag{12}$$

We partition the spatial domain into the grid cells $I_j := [x_{j-\frac{1}{2}}, x_{j+\frac{1}{2}}]$, where Δx is the spatial scale, $x_{j\pm\frac{1}{2}} = x_j \pm \frac{\Delta x}{2}$ and x_j is the center of the grid cell. Let us denote by $\bar{\mathbf{v}}_j(t)$ the computed cell average of $\mathbf{v}(x, t)$ over the cell I_j,

$$\bar{\mathbf{v}}_j(t) = \frac{1}{\Delta x}\int_{x_{j-\frac{1}{2}}}^{x_{j+\frac{1}{2}}} \mathbf{v}(x,t)\,dx. \tag{13}$$

Integrating Eq. (10) over each cell I_j, we obtain the semidiscrete formulation

$$\frac{d}{dt}\bar{\mathbf{v}}_j(t) + \frac{1}{\Delta x}\Big(\mathbf{f}(\mathbf{v}(x_{j+\frac{1}{2}},t)) - \mathbf{f}(\mathbf{v}(x_{j-\frac{1}{2}},t))\Big) = \frac{1}{\Delta x}\int_{x_{j-\frac{1}{2}}}^{x_{j+\frac{1}{2}}} \mathbf{S}(\mathbf{v}(x,t),x)\;dx, \tag{14}$$

which is approximated by

$$\frac{d}{dt}\bar{\mathbf{v}}_j(t) = -\frac{\mathbf{H}_{j+\frac{1}{2}} - \mathbf{H}_{j-\frac{1}{2}}}{\Delta x} + \frac{1}{\Delta x}\int_{x_{j-\frac{1}{2}}}^{x_{j+\frac{1}{2}}} \mathbf{S}(\mathbf{v},x)\,dx. \tag{15}$$

Here $\mathbf{H}_{j\pm\frac{1}{2}}$ is the numerical flux at the cell interfaces $x_{j\pm\frac{1}{2}}$. Typical semidiscrete central-upwind schemes consider flux values at the interfaces obtained by non-oscillatory polynomial reconstructions. The non-oscillatory behavior is usually achieved by the use of nonlinear limiters, as in Kurganov and Tadmor (2000). Higher order approximations require the implementation of expensive and complicated nonlinear limiters. An alternative procedure requires the use of artificial viscosity, proposed in Chen et al. (2013). We incorporate those ideas to the shallow-water flows in channels. The artificial viscosity is added to the system, and Eq. (10) becomes

$$\mathbf{v}_t + \mathbf{f}(\mathbf{v})_x = \mathbf{S}(\mathbf{v},x) + (\epsilon(\mathbf{v})\mathbf{v}_x)_x, \tag{16}$$

where $\boldsymbol{\epsilon}(\mathbf{v})$ vanishes as we refine the grid. This assures that the resulting method is consistent with the system. The resulting approximation in (15) becomes

$$\frac{d}{dt}\bar{\mathbf{v}}_j(t) = -\frac{\mathbf{H}_{j+\frac{1}{2}} - \mathbf{H}_{j-\frac{1}{2}}}{\Delta x} + \frac{1}{\Delta x}\int_{x_{j-\frac{1}{2}}}^{x_{j+\frac{1}{2}}} \mathbf{S}(\mathbf{v},x)\,dx + C\left(\frac{\epsilon_{j+\frac{1}{2}}\Delta\bar{\mathbf{v}}_{j+\frac{1}{2}} - \epsilon_{j-\frac{1}{2}}\Delta\bar{\mathbf{v}}_{j-\frac{1}{2}}}{(\Delta x)^2}\right), \tag{17}$$

where $\Delta\bar{\mathbf{v}}_{j\pm\frac{1}{2}} = \bar{\mathbf{v}}_{j\pm\frac{1}{2}+\frac{1}{2}} - \bar{\mathbf{v}}_{j\pm\frac{1}{2}-\frac{1}{2}}$. Here C is a positive viscosity coefficient whose size is adjusted depending on the local properties of the primitive variables of our system.

The flux at the cell interfaces, $\mathbf{f}(\mathbf{v}(x_{j\pm\frac{1}{2}}),t)$, is approximated by the numerical flux $\mathbf{H}_{j\pm\frac{1}{2}}(t)$ given by, ,

$$\mathbf{H}_{j\pm\frac{1}{2}}(t) = \frac{a^+_{j\pm\frac{1}{2}}\mathbf{f}\Big(\mathbf{v}^-_{j\pm\frac{1}{2}}(t)\Big) - a^-_{j\pm\frac{1}{2}}\mathbf{f}\Big(\mathbf{v}^+_{j\pm\frac{1}{2}}(t)\Big)}{a^+_{j\pm\frac{1}{2}} - a^-_{j\pm\frac{1}{2}}} + \frac{a^+_{j\pm\frac{1}{2}}a^-_{j\pm\frac{1}{2}}}{a^+_{j\pm\frac{1}{2}} - a^-_{j\pm\frac{1}{2}}}\Big(\mathbf{v}^+_{j\pm\frac{1}{2}}(t) - \mathbf{v}^-_{j\pm\frac{1}{2}}(t)\Big), \tag{18}$$

where the one-sided local speeds in this scheme are approximated using the eigenvalues of the Jacobian:

$$a^+_{j\pm\frac{1}{2}} = \max\left\{u^+_{j\pm\frac{1}{2}} + c^+_{j\pm\frac{1}{2}}, u^-_{j\pm\frac{1}{2}} + c^-_{j\pm\frac{1}{2}}, 0\right\}$$
$$a^-_{j\pm\frac{1}{2}} = \min\left\{u^+_{j\pm\frac{1}{2}} - c^+_{j\pm\frac{1}{2}}, u^-_{j\pm\frac{1}{2}} - c^-_{j\pm\frac{1}{2}}, 0\right\}. \tag{19}$$

We note that $a^+_{j\pm\frac{1}{2}} - a^-_{j\pm\frac{1}{2}} > 0$ is always positive unless $h^\pm_{j\pm\frac{1}{2}}, u^\pm_{j\pm\frac{1}{2}}$ all vanish in a dry state with "no fluid motion". However, we always start with positive values of h. Even in dam-break problems, initial dry states are represented by a threshold (see Eq. (50)). Furthermore, the velocity is given by the regularization process in (35) near dry states, and it is usually not negligible.

The last term in Eq. (16) is ignored in second order semidiscrete central-upwind scheme with polynomial reconstructions and nonlinear limiters. Their higher order versions require more complicated and computationally expensive techniques when nonlinear limiters are used. Here, the interface point-values $\mathbf{v}^\pm_{j\pm\frac{1}{2}}(t)$ are recovered from a non-limited conservative fifth order piecewise polynomial reconstruction as in Kurganov and Liu (2012)

$$r^+_{j+\frac{1}{2}} := \frac{1}{60}(-3\bar{r}_{j-1} + 27\bar{r}_j + 47\bar{r}_{j+1} - 13\bar{r}_{j+2} + 2\bar{r}_{j+3}),$$
$$r^-_{j+\frac{1}{2}} := \frac{1}{60}(2\bar{r}_{j-2} - 13\bar{r}_{j-1} + 47\bar{r}_j + 27\bar{r}_{j+1} - 3\bar{r}_{j+2}), \tag{20}$$

where $r \in \{w, Q\}$. From the reconstructed w and Q, we can recover the rest of the variables according to the definitions above. For instance, the cross-sectional wet area is given by $A^\pm_{j+\frac{1}{2}} = \int_{B_{j+\frac{1}{2}}}^{w^\pm_{j+\frac{1}{2}}} \sigma(x_{j+\frac{1}{2}}, z)dz$. We note that A is a strictly increasing function of w because $\sigma(x, z) \geq 0$. The dependance of A in w might be complicated if σ is non-trivial. In practice, each cross section is considered piecewise trapezoidal. We can then numerically invert the formula to recover w from A when needed.

The artificial viscosity in Eq. (16) is discretized in Chen et al. (2013) by plugging in the approximated solution in a discretized equation and computing the residual, at time t and $t - \Delta t$, to obtain $\boldsymbol{\epsilon}$. The diffusion coefficient $\boldsymbol{\epsilon}$ obtained this way, as numerically observed in Kurganov and Liu (2012), satisfies $\epsilon = O(\Delta x)$ near shock waves, $\epsilon = O(\Delta x^\alpha), 1 < \alpha < 2$ near contact waves, and $\epsilon = O(\Delta x^p), p = \min(r+2, 4)$, in smooth regions, where r is the formal order of accuracy of the scheme. For the sake of simplicity, we consider

$$\epsilon^1_{j+\frac{1}{2}} = \Delta x\left(\frac{|w_j - w_{j-1}|}{[w]}\right)^{\frac{r-1}{2}}, \epsilon^2_{j+\frac{1}{2}} = \Delta x\left(\frac{|Q_j - Q_{j-1}|}{[Q]}\right)^{\frac{r-1}{2}}, \tag{21}$$

where $\epsilon^1_{j+\frac{1}{2}}, \epsilon^2_{j+\frac{1}{2}}$ are applied to the first and second entries of equation (1) respectively, $[w]$, $[Q]$ are reference scales for the total height w and discharge Q, and r is the formal order of accuracy of the scheme. The reference scales are kept constant in space and time. We choose the total height in the approximation of $\epsilon_{j+\frac{1}{2}}$ instead of the conserved variable A to maintain well-balance, as explained below. The diffusion coefficient $\epsilon_{j+\frac{1}{2}}$, is approximated at $x_{j+\frac{1}{2}}$ using a centered difference approximation for the derivative of w and Q. Formally, $\epsilon = O(\Delta x)$ near shock waves and $\epsilon = O(\Delta x^r)$ in smooth regions. In practice, C is a positive viscosity coefficient whose size is adjusted depending on the local properties of the primitive variables, as explained in Chen et al. (2013).

Desirable properties in the scheme such as precision near shock waves, well-balance, and positivity are all coupled with each other and to the geometry and topography. Achieving particular properties may be more difficult in some numerical approaches than in others. Putting all properties together in one might be even harder. Replacing nonlinear limiters by artificial viscosity requires adapting and fitting this new term in all of the properties and considerations. In the rest of this section, we describe how we incorporate artificial viscosity and high resolution to the proposed central-upwind scheme while still preserving all the other desirable properties.

3.2. Well balance property of the proposed numerical scheme

A scheme for shallow-water flows is said to be well-balanced if it is able to preserve steady-state flows at rest. The first equation is

easy to treat because $Q = 0$ at rest. In the second equation, there has to be a balance between the flux gradient and the source term. The discretization of the source term has to be carefully chosen so as to balance with the numerical flux gradient in Eq. (17) in those flows. Reconstructing the point-values from the data $\{\overline{w}_j\}$ instead of $\{\bar{A}_j\}$ is a key point in the well-balance property. In a "lake at rest", the total height $\overline{w}_j$ is constant while $\bar{A}_j$ changes. In this situation, the reconstruction from $\{\overline{w}_j\}$ is trivial. This is a first step in achieving the well-balance property. As it can be observed in Eq. (21), the adaptive viscosity coefficients ϵ^1, ϵ^2 vanish in steady states at rest since w is constant throughout the domain, and the discharge vanishes. The numerical artificial viscosity treated this way does not affect the well-balance property.

We will often use the discretized form of Leibniz's rule for differentiation under the integral sign, which states that

$$\Delta\left[\int_{a(x)}^{b(x)} f(x,z)\,dz\right] = \frac{1}{2}\left(\int_{a_L}^{b_L} + \int_{a_R}^{b_R}\right)\Delta[f(\cdot,z)]\,dz + \int_{b_L}^{b_R}\overline{f}(z)\,dz - \int_{a_L}^{a_R}\overline{f}(z)\,dz, \tag{22}$$

where $(\cdot)_L(z) = (\cdot)(x_L, z)$, $(\cdot)_R(z) = (\cdot)(x_R, z)$, $\Delta[f(\cdot,z)] = f(x_R,z) - f(x_L,z)$, $\overline{f}(z) = \frac{f_L(z)+f_R(z)}{2}$.

Consider a steady state at rest $w = Const.$, $u = 0$. Applying the rule above, the flux difference amounts to

$$\frac{H^Q_{j+\frac{1}{2}} - H^Q_{j-\frac{1}{2}}}{\Delta x} = \frac{1}{\Delta x}\frac{g}{2}\left(\int_{B_{j-\frac{1}{2}}}^{w_{j-\frac{1}{2}}} + \int_{B_{j+\frac{1}{2}}}^{w_{j+\frac{1}{2}}}\right)\Delta[(w-z)\sigma](z)dz + \frac{1}{\Delta x}g\int_{w_{j-\frac{1}{2}}}^{w_{j+\frac{1}{2}}}\overline{(w-z)\,\sigma(x,z)}dz - \frac{1}{\Delta x}g\int_{B_{j-\frac{1}{2}}}^{B_{j+\frac{1}{2}}}\overline{(w-z)\,\sigma(x,z)}\,dz$$

The second term in the right-hand side vanishes when w is constant. Ignoring that term, we obtain a consistent discretization of the source term

$$\overline{S}^Q_j(t) = \frac{1}{\Delta x}\frac{g}{2}\left(\int_{B_{j-\frac{1}{2}}}^{w_{j-\frac{1}{2}}} + \int_{B_{j+\frac{1}{2}}}^{w_{j+\frac{1}{2}}}\right)(w_j - z)\Delta\sigma_j(z)dz - \frac{1}{\Delta x}g\int_{B_{j-\frac{1}{2}}}^{B_{j+\frac{1}{2}}}(w_j - z)\,\overline{\sigma}_j(z)\,dz, \tag{23}$$

which ensures a balance with the flux differences in steady states at rest.

3.3. Time evolution of the numerical scheme

Since we have used a high order spatial discretization, it is sensible to use a high order time discretization as well. Once the flux gradient and the averaged source terms are calculated, the ODE system (15) is integrated in time using the third order Strong Stability Preserving Runge–Kutta scheme (Gottlieb et al., 2001),

$$\overline{\mathbf{v}}_1^{(n+1)} = \overline{\mathbf{v}}^{(n)} + \Delta t\,\mathbf{RK}[\overline{\mathbf{v}}^{(n)}] \tag{24a}$$

$$\overline{\mathbf{v}}_2^{(n+1)} = \frac{3}{4}\overline{\mathbf{v}}^{(n)} + \frac{1}{4}\left(\overline{\mathbf{v}}_1^{(n+1)} + \Delta t\,\mathbf{RK}[\overline{\mathbf{v}}_1^{(n+1)}]\right) \tag{24b}$$

$$\overline{\mathbf{v}}^{(n+1)} := \frac{1}{3}\overline{\mathbf{v}}^{(n)} + \frac{2}{3}\left(\overline{\mathbf{v}}_2^{(n+1)} + \Delta t\,\mathbf{RK}[\overline{\mathbf{v}}_2^{(n+1)}]\right) \tag{24c}$$

with the Runge–Kutta fluxes

$$\mathbf{RK}[\mathbf{v}(t)] = -\frac{\mathbf{H}_{j+\frac{1}{2}}(\mathbf{v}(t)) - \mathbf{H}_{j-\frac{1}{2}}(\mathbf{v}(t))}{\Delta x} + \overline{\mathbf{S}}_j(t) + C\left(\frac{\epsilon_{j+\frac{1}{2}}\Delta\overline{\mathbf{v}}_{j+\frac{1}{2}} - \epsilon_{j-\frac{1}{2}}\Delta\overline{\mathbf{v}}_{j-\frac{1}{2}}}{(\Delta x)^2}\right). \tag{25}$$

Here $\overline{\mathbf{S}}_j(t)$ is calculated according to (23). The time step Δt is determined so as to satisfy a *CFL* restriction. As described in Proposition 1, a separate restriction on the time step Δt is needed to ensure positivity. We verify that such restriction is met in each of the stages (24a),(24b), and (24c).

3.4. Positivity-preserving property

The interface values $h^{\pm}_{j\pm\frac{1}{2}} = w^{\pm}_{j\pm\frac{1}{2}} - B_{j\pm\frac{1}{2}}$ obtained with the fifth order reconstruction (20) does not guarantee the positivity of $h^{\pm}_{j\pm\frac{1}{2}}$, or equivalently, $A^{\pm}_{j\pm\frac{1}{2}} \geq 0$, which is important for the positivity-preserving property in the water's depth time evolution. To prevent this numerical artifact, we follow (Kurganov and Petrova, 2007) and check the reconstructed point-values $w^{\pm}_{j\pm\frac{1}{2}}$, correcting them –if necessary– as follows

$$\text{if } w^+_{j-\frac{1}{2}} < B_{j-\frac{1}{2}} + h_\delta \Longrightarrow \begin{cases} w^+_{j-\frac{1}{2}} = B_{j-\frac{1}{2}} + h_\delta, \\ w^-_{j+\frac{1}{2}} = \overline{w}_j + \frac{1}{2}w'_j, \\ \quad \text{where } w'_j = 2(\overline{w}_j - B_{j-\frac{1}{2}} - h_\delta), \end{cases} \tag{26}$$

else

$$\text{if } w^-_{j+\frac{1}{2}} < B_{j+\frac{1}{2}} + h_\delta \Longrightarrow \begin{cases} w^-_{j+\frac{1}{2}} = B_{j+\frac{1}{2}} + h_\delta, \\ w^+_{j-\frac{1}{2}} = \overline{w}_j - \frac{1}{2}w'_j, \\ \quad \text{where } w'_j = 2(B_{j+\frac{1}{2}} + h_\delta - \overline{w}_j), \end{cases} \tag{27}$$

which yields

$$h^-_{j+\frac{1}{2}} := w^-_{j+\frac{1}{2}} - B_{j+\frac{1}{2}} \geq 0, \tag{28}$$

and

$$h^+_{j-\frac{1}{2}} := w^+_{j-\frac{1}{2}} - B_{j-\frac{1}{2}} \geq 0. \tag{29}$$

Here $h_\delta = 10^{-5}$ is a threshold we use in the positivity of the water's depth. We note that this goes back to the second order reconstruction which is used only near dry states. This approximation does not have a large impact on the global accuracy of the proposed scheme.

The correction to the reconstruction in Eqs. (26) and (27) guarantees the positivity of the reconstructed interface values but it does not guarantee the positivity of the solution at the next time step. We need one more correction in some cases (see the proof of the proposition below). Following (Chen et al., 2013), the second correction can be explained by defining

$$\hat{A}_j = 3\overline{A}_j - A^-_{j+\frac{1}{2}} - A^+_{j-\frac{1}{2}}, \tag{30}$$

which is yet another approximation for $A(x_j, t)$, and it will be negative only near dry states. In that situation, we correct the reconstruction at the cell interfaces by distributing the wet area to make $\hat{A}_j$ vanish instead of being negative. We note that if $\hat{A}_j$ is negative,

$A^-_{j+\frac{1}{2}} + A^+_{j-\frac{1}{2}} \geq -\hat{A}_j$, so at least one of the interface values $A^-_{j+\frac{1}{2}}$ or $A^+_{j-\frac{1}{2}}$ have to be greater than $-\hat{A}_j/2$. The second correction is then as follows

$$\text{If } \hat{A}_j < 0, \text{ redefine } \begin{cases} \text{if } \min(A^-_{j+\frac{1}{2}}, A^+_{j-\frac{1}{2}}) \geq -\hat{A}_j/2, & \hat{A}^-_{j+\frac{1}{2}} = A^-_{j+\frac{1}{2}} + \hat{A}_j/2, & \hat{A}^+_{j-\frac{1}{2}} = A^+_{j-\frac{1}{2}} + \hat{A}_j/2 \\ \text{if } A^+_{j-\frac{1}{2}} \leq -\hat{A}_j/2 \leq A^-_{j+\frac{1}{2}}, & \hat{A}^-_{j+\frac{1}{2}} = 3\overline{A}_j, & \hat{A}^+_{j-\frac{1}{2}} = 0, \\ \text{if } A^-_{j+\frac{1}{2}} \leq -\hat{A}_j/2 \leq A^+_{j-\frac{1}{2}}, & \hat{A}^-_{j+\frac{1}{2}} = 0, & \hat{A}^+_{j-\frac{1}{2}} = 3\overline{A}_j, \end{cases} \tag{31}$$

and recover $w^-_{j+\frac{1}{2}}, w^+_{j-\frac{1}{2}}$ from $\hat{A}^-_{j+\frac{1}{2}}$ and $\hat{A}^+_{j-\frac{1}{2}}$. (32)

Central-upwind schemes usually compute its time step according to a CFL condition

$$\text{CFL} = \frac{a\Delta t}{\Delta x} \leq \frac{1}{2}, \tag{33}$$

where $a = \max_j(a^+_{j+\frac{1}{2}}, -a^-_{j+\frac{1}{2}})$, and CFL is known as the Courant number. In order to satisfy the positivity-preserving property (Proposition 1 below), a more restrictive condition is required

$$\text{CFL}_\epsilon = \max(a, 2C\max_j \epsilon_{j\pm\frac{1}{2}}/\Delta x)\ \frac{\Delta t}{\Delta x} \leq \frac{1}{2}, \tag{34}$$

where CFL_ϵ is a modified Courant number.

3.5. Regularization of flow velocity and discharge for small A

While the reconstruction and corrections described above guaranties positivity of the water's depth at the cell interfaces, these point-values may still be very small (*i.e.*, arbitrarily close to zero) and may lead to large values of the velocity of the flow, u. We can prevent this with a regularization technique suggested by Kurganov and Petrova (2007),

$$u^\pm_{j\pm\frac{1}{2}} = \frac{\sqrt{2}\,Q^\pm_{j\pm\frac{1}{2}} A^\pm_{j\pm\frac{1}{2}}}{\sqrt{\left(A^\pm_{j\pm\frac{1}{2}}\right)^4 + \max\left((A^\pm_{j\pm\frac{1}{2}})^4, \delta^4\right)}}, \tag{35}$$

with

$$A^\pm_{j\pm\frac{1}{2}} = \int_{B_{j\pm\frac{1}{2}}}^{w^\pm_{j\pm\frac{1}{2}}} \sigma_{j\pm\frac{1}{2}}(z)\,dz, \qquad \sigma_{j\pm1/2}(z) := \sigma(x_{j\pm1/2}, z). \tag{36}$$

For consistency, the discharge has to be recalculated as

$$Q^\pm_{j\pm\frac{1}{2}} = A^\pm_{j\pm\frac{1}{2}} u^\pm_{j\pm\frac{1}{2}}. \tag{37}$$

The value of δ was empirically determined, usually choosing $\delta = \Delta x$ in this paper.

Each desirable property has been analyzed separately. We now show that all properties can be put together, as stated in the following proposition.

Proposition 1. *Let $B_{j\pm\frac{1}{2}} = B(x_{j\pm\frac{1}{2}})$, and $\sigma_{j\pm\frac{1}{2}}(z) = \sigma(x_{j\pm\frac{1}{2}}, z)$ be the topography and geometry at the interfaces $x_{j\pm\frac{1}{2}}$, and define the following approximation of the cell average $\overline{S}^Q_j$ in (23)*

$$\frac{1}{\Delta x}\int_{x_{j-\frac{1}{2}}}^{x_{j+\frac{1}{2}}}\int_B^w g\,(w-z)\,\sigma_x(x,z)\,dz\,dx \approx \frac{1}{\Delta x}\frac{g}{2}\left(\int_{B_{j-\frac{1}{2}}}^{w^+_{j-\frac{1}{2}}} + \int_{B_{j+\frac{1}{2}}}^{w^-_{j+\frac{1}{2}}}\right)\left(\overline{w}_j - z\right)\Delta\sigma_j(z)\,dz, \tag{38}$$

and

$$\frac{1}{\Delta x}\int_{x_{j-\frac{1}{2}}}^{x_{j+\frac{1}{2}}} g\,\sigma_B(x)\,hB_x\,dx \approx \frac{g}{\Delta x}\int_{B_{j-\frac{1}{2}}}^{B_{j+\frac{1}{2}}}\left(\overline{w}_j - z\right)\overline{\sigma}_j(z)\,dz, \tag{39}$$

where $w^\pm_{j\mp\frac{1}{2}}$ are the reconstructed point-values of $w = h + B$ at the interfaces $x_{j\pm\frac{1}{2}}$ (in the interior of the cell I_j),

$$\Delta\sigma_j(z) = \sigma_{j+\frac{1}{2}}(z) - \sigma_{j-\frac{1}{2}}(z), \quad \text{and} \quad \overline{\sigma}_j(z) = \frac{\sigma_{j-\frac{1}{2}}(z) + \sigma_{j+\frac{1}{2}}(z)}{2}.$$

Then the scheme (15)–(18) is well balanced. Furthermore, consider the corrections (26), (27), (31) and (32), and the CFL condition (34). If the cell averages $A(t)$ are such that

$$\overline{w}_j(t) \geq \frac{B_{j-\frac{1}{2}} + B_{j+\frac{1}{2}}}{2} \qquad \forall j,$$

then the cell averages $A(t+\Delta t)$ as evolved with forward Euler's method (24a), under the CFL limitation (34) with

$$a^+_{j\pm\frac{1}{2}} = \max\{u^+_{j\pm\frac{1}{2}} + c_{j\pm\frac{1}{2}}+, u^-_{j\pm\frac{1}{2}} + c^-_{j\pm\frac{1}{2}}, 0\}, c^+_{j\pm\frac{1}{2}} = \sqrt{g\frac{A^+_{j\pm\frac{1}{2}}}{\sigma^{T,+}_{j\pm\frac{1}{2}}}}, \quad \text{and} \quad \sigma^{T,+}_{j\pm\frac{1}{2}} = \sigma\left(x_{j\pm\frac{1}{2}}, w^+_{j\pm\frac{1}{2}}\right), \tag{40}$$

will yield

$$\overline{w}_j(t+\Delta t) \geq \frac{B_{j-\frac{1}{2}} + B_{j+\frac{1}{2}}}{2} \qquad \forall j.$$

Proof. The well-balance property was already shown and the corrections do not have any impact on it. For the positivity of the scheme, and defining $\lambda = \frac{\Delta t}{\Delta x}$, the updated cell average of the wet area A satisfies

$$\begin{aligned}\overline{A}_j(t+\Delta t) = \overline{A}_j &- \frac{\lambda(a^+_{j+\frac{1}{2}}A^-_{j+\frac{1}{2}}u^-_{j+\frac{1}{2}} - a^-_{j+\frac{1}{2}}A^+_{j+\frac{1}{2}}u^+_{j+\frac{1}{2}} + a^+_{j+\frac{1}{2}}a^-_{j+\frac{1}{2}}(A^+_{j+\frac{1}{2}} - A^-_{j+\frac{1}{2}}))}{a^+_{j+\frac{1}{2}} - a^-_{j+\frac{1}{2}}} \\ &+ \frac{\lambda(a^+_{j-\frac{1}{2}}A^-_{j-\frac{1}{2}}u^-_{j-\frac{1}{2}} - a^-_{j-\frac{1}{2}}A^+_{j-\frac{1}{2}}u^+_{j-\frac{1}{2}} + a^+_{j-\frac{1}{2}}a^-_{j-\frac{1}{2}}(A^+_{j-\frac{1}{2}} - A^-_{j-\frac{1}{2}}))}{a^+_{j-\frac{1}{2}} - a^-_{j-\frac{1}{2}}} \\ &+ \frac{C\lambda}{\Delta x}\left(\epsilon_{j+\frac{1}{2}}A_{j+1} + \epsilon_{j-\frac{1}{2}}A_{j-1}\right) - \frac{C\lambda}{\Delta x}A_j(\epsilon_{j+\frac{1}{2}} + \epsilon_{j-\frac{1}{2}}),\end{aligned}$$

which can be rewritten as

$$\begin{aligned}\overline{A}_j(t+\Delta t) = \frac{1}{4}\hat{A}_j &+ \left[\frac{1}{4} - \lambda a^+_{j+\frac{1}{2}}\frac{u^-_{j+\frac{1}{2}} - a^-_{j+\frac{1}{2}}}{a^+_{j+\frac{1}{2}} - a^-_{j+\frac{1}{2}}}\right]A^-_{j+\frac{1}{2}} \\ &+ \left[\frac{1}{4} + \lambda a^-_{j-\frac{1}{2}}\frac{a^+_{j-\frac{1}{2}} - u^+_{j-\frac{1}{2}}}{a^+_{j-\frac{1}{2}} - a^-_{j-\frac{1}{2}}}\right]A^+_{j-\frac{1}{2}} \\ &- \lambda a^-_{j+\frac{1}{2}}\frac{a^+_{j+\frac{1}{2}} - u^+_{j+\frac{1}{2}}}{a^+_{j+\frac{1}{2}} - a^-_{j+\frac{1}{2}}} + \lambda a^+_{j-\frac{1}{2}}\frac{u^-_{j-\frac{1}{2}} - a^-_{j-\frac{1}{2}}}{a^+_{j-\frac{1}{2}} - a^-_{j-\frac{1}{2}}} \\ &+ \frac{C\lambda}{\Delta x}\left[\epsilon_{j+\frac{1}{2}}A_{j+1} + \epsilon_{j-\frac{1}{2}}A_{j-1}\right] \\ &+ \left[\frac{1}{4} - \frac{C\lambda}{\Delta x}(\epsilon_{j+\frac{1}{2}} + \epsilon_{j-\frac{1}{2}})\right]\overline{A}_j\end{aligned}$$

and applying the *CFL* restriction (34), we conclude the proof. □

Note: The positivity is still valid in any time integration which is a convex combination (with nonnegative coefficients) of Euler steps such as in RK3 (Shu and Osher, 1989).

4. Numerical results

In this section, we present the numerical results obtained with the proposed scheme, choosing a variety of tests to show its merits. Each test chosen is aimed at demonstrating different aspects and properties of the numerical approach. In some of the tests, comparisons with other alternatives are considered. In the first numerical test, a perturbation to a steady state at rest is taken to illustrate the importance of the well-balance property. Following this, we analyze the convergence to more general steady states for long periods of time. Here we select both subcritical flows and transcritical flows with stationary shock waves. The positivity-preserving property is then examined for three dam-break problems. The first test is a numerical experiment to test the aforementioned property. The last two examples were taken from a real laboratory experiment, and comparisons with our numerical solutions are shown. The acceleration of gravity is $g = 9.81$, unless otherwise stated.

4.1. Perturbations of steady state of rest and efficiency test

Proposition 1 shows that if we start with a "lake at rest" ($h + B$ constant, $u = 0$), the scheme will recognize and respect such equilibrium, regardless of the complicated geometry or topography. We argue that such property enables the scheme to accurately compute near steady state flows. In particular, if we introduce a perturbation to the state at rest, we expect the perturbation to evolve and eventually leave the domain, recovering the initial state. Schemes that do not respect such equilibrium relations might present large errors when trying to converge at large computational times. The initial conditions are given by

$$u(x, t=0) = 0,\ w(x, t=0) = \begin{cases} h_{\text{out}} & \text{if } x \in [0,1] \setminus [0.4, 0.5] \\ h_{\text{out}} + \epsilon & \text{if } x \in [0.4, 0.5] \end{cases}, \tag{41}$$

where $h_{\text{out}} = 1.1, \epsilon = 0.3$. The perturbation for the steady state at rest is given by the parameter ϵ. Numerical schemes that are not in balance might generate numerical errors of the same order of magnitude as the perturbation itself. Here we test the numerical scheme for flows that are near steady states.

The physical domain in the horizontal x-direction is [0, 1], and the topography and geometry are given by

$$\begin{aligned} B(x) &= \max\left(1 - 8\left(x - \frac{1}{2}\right)^2, 0\right), \sigma(x, z) \\ &= 1 - 0.8\exp\left(-5\left(x - \frac{1}{2}\right)^2 - 5(z-1)^2\right). \end{aligned} \tag{42}$$

Regarding the artificial viscosity constant, $C = 100$ is chosen in all numerical tests unless otherwise stated. Following (Chen et al., 2013; Guermond et al., 2011; Kurganov and Liu, 2012) the value of C was tuned using a very coarse mesh to estimate the smallest value that best controls the oscillations. Once that value is estimated, we then proceed with the high resolution simulations on finer meshes. Free boundary conditions are used for this simulation. Fig. 2 shows the numerical evolution of the perturbation at time $t = 0.05$, using a resolution of $\Delta x = 1/500$. The solid black line denotes the topography. The red dashed line represents the computed solution using the proposed scheme. Exact solutions to perturbations from steady states at rest are not available in general. For comparison, we compute a separate approximation using the Roe-type upwind scheme as in Hernández-Dueñas and Karni (2011), which uses nonlinear limiters. Small differences due to the high-order reconstruction can be observed. To quantify the differences, we compute a "relative error". That is, for any quantity q defined on a domain $[a, b]$, the relative error, using the L^2 norm, is computed as

$$\text{err}(t) = \sqrt{\frac{1}{b-a}\int_a^b \left(\frac{q(x,t) - q_{\text{ref}}(x,t))}{q_{\text{ref}}(x,t)}\right)^2 dx}, \tag{43}$$

where q_{ref} is the exact solution or reference quantity. The relative error for the total height computed according to (43) is 1.2×10^{-3} at $t = 0.05$, with a maximum value of 2.1×10^{-2}. The artificial viscosity is acting only where needed, and the shock wave is correctly captured, as the comparison indicates. One can get a better sense of the channel's shape in the 3D view of the channel in the right panel. The interplay between the topography and the walls, which affects the evolution of the flow is evident in that plot.

We have claimed that the adaptive artificial viscosity offers a high order accuracy at a low computational cost, and this is the original motivation in Chen et al. (2013), Kurganov and Liu (2012). Here we compare the computational cost of the current method and the upwind scheme. The time step for all the numerical tests are computed according to the condition in (34), with a modified Courant number of $\text{CFL}_\epsilon = 0.45$. In both schemes, the time step is about $\Delta t = 2.34 \times 10^{-4}$, which indicates that the time step condition (34) is not reducing the time step according to the standard CFL condition (33). Fixing that time step, the CPU time for the current scheme is 44.2 s. Regarding the upwind scheme, we have used the same Courant number and RK3 time integration to fairly compare the computational cost. The CPU time for the reference Roe-type upwind scheme is 58.0 s. We have then achieved higher order approximations at a lower computational cost in this numerical test.

4.2. Convergence to smooth subcritical steady states

A delicate balance between the geometry, topography and the flux gradients give rise to a variety of interesting steady states besides those at rest considered in the previous section. Smooth steady states satisfy that both the discharge Q and the energy E are constant throughout the domain, as indicated by Eq. (7). The expressions for both quantities provide a way to compute such flows as follows. Given Q, E, $B(x)$, $\sigma(x, \cdot)$, one needs to solve the equation in h

$$\frac{1}{2}Q^2 + (g(h + B) - E)A^2 = 0, \tag{44}$$

where $A = A(h) = \int_B^{h+B} \sigma(x, z)dz$. The wet area A is an increasing function of h. As a result, in general we have only three roots available. One can choose the physically relevant root according to restrictions such as positivity and Froude numbers (subcritical or supercritical flows). Cooked-up solutions are available with this procedure.

Under appropriate boundary conditions, a flow must converge to a steady state for long computational times. In our case, one imposes the corresponding discharge Q_{in} of the cooked-up steady-state solution and extrapolates h at the left boundary. Here Q_{in} is the constant discharge chosen a priory in Eq. (44). At the right boundary, we extrapolate Q. Furthermore, we impose h_{out} at inflow ($u - c < 0$) and extrapolate h at outflow ($u - c \geq 0$). Here h_{out} is the outward water's depth of the equilibrium state. The water's depth h_{out} is special in the sense that any other value imposed at the boundary creates equilibrium states that jump somewhere in the domain to match the right boundary condition. Of course the flow jumps where the Rankine-Hugoniot conditions are satisfied. Such scenario is the topic of the next numerical test.

We illustrate the merits of incorporating the well-balance property in the numerical scheme. One important consequence of recognizing steady states at rest is the ability of the scheme to be

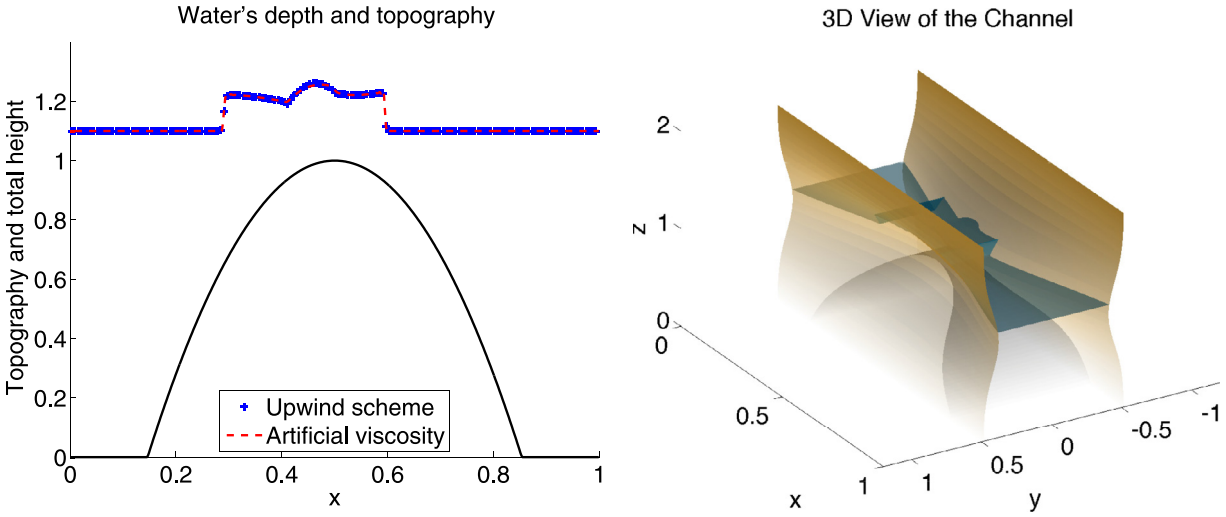

Fig. 2. Perturbation from a steady state at rest at $t = 0.05$. Left: 2D view of the numerical results with an upwind scheme (blue "+" signs) and the proposed scheme using artificial viscosity (red dashed line). The topography is in solid black. Right: 3D-view showing the topography at the bottom (grey), the walls ("camel" color) and the water's total height (light blue). (For interpretation of the references to colour in this figure legend, the reader is referred to the web version of this article.)

much more accurate near those steady states. It also seems to help in accurately computing steady states that are not in rest.

In the test case here, we start our simulation with the following initial conditions

$$\begin{cases} w(x,0) = B(x) + h(x,0) = w_{\text{out}} = 0.8, \\ u(x,0) = 0, \end{cases} \tag{45}$$

imposing $Q_{\text{in}} = 0.3343$ at inflow and $h_{\text{out}} = 0.8$ at outflow, as described above. The topography is given by a spline of degree three with nodes (0.2, 0) ,(0.3, 0.6), (0.4, 0.4), (0.5, 0.5), (0.6, 0.2), (0.7, 0) in the domain $x \in [0, 1]$.

The geometry is given by

$$\sigma(x,z) = \left(1 + \frac{3}{4}\cos(\pi x)\right)\left(1 - \frac{z}{2}\right), \quad 0 \le x \le 1, 0 \le z \le H_{\max} = 2. \tag{46}$$

There is a unique subcritical steady-state flow with the given conditions. Such solution has constant energy $E_{\text{out}} = 10.0748$ and can be computed exactly by solving Eq. (44). The exact solution will be used for comparison with the numerical solution to evaluate the precision of the scheme computing near steady-state flows. The left panel of Fig. 3 shows the topography, and the total water's surface w at time $T = 20$, with a resolution of $\Delta x = 1/200$. The blue "+" signs indicate the exact steady state solution. By looking at the exact and numerical water's surface, we see that the two graphs are on top of each other. A more detailed analysis of the numerical error is conducted below. The computed solutions are oscillation-free and highly resolved which demonstrates the ability of the proposed method to accurately capture quasi-steady state solutions.

The computational time is long to allow for convergence to a steady state, with a CPU time of 3.1×10^3 s. The time steps given by (33) and (34) vary from 5.8×10^{-4} s to 7.5×10^{-4} s and from 4.8×10^{-4} s to 7.5×10^{-4} s respectively. The final time steps levels off at about 4.95×10^{-4}. The extra constraint in the CFL condition in (34) did not significantly decrease the time step in this test. The right panel provides a 3D view of the channel. The grey surface denotes the topography. The channel walls are in "camel" color, and the total surface's height in light blue. The channel narrows down towards the end of it, causing the flow to accelerate and reduce its total height.

Fig. 4 exhibits more details of the simulations. A challenging measure for convergence to steady states is the relative error of the final discharge and energy. The corresponding graphs for smooth steady state flows are flat. Other measures may extend vertically and small errors might be hard to visualize. For the current numerical test, the top panel of Fig. 4 shows final discharge of the numerical solution (dashed red line) and the exact value of the discharge Q_{in} (blue "+" signs) . We see small variations of the discharge that might misleadingly seem large. However, the relative error for the final discharge computed according to (43) is 5.77×10^{-4} using the L^2 norm, with a maximum value of 1.8×10^{-3}. The figure's vertical axis extends 1% in each direction, $[0.99Q_{\text{in}}, 1.01Q_{\text{in}}]$. The bottom panel shows the equivalent quantities for the energy of the solution. The corresponding relative error is 6.21×10^{-5}, with a maximum of 1.4×10^{-4}, which is much smaller than the final discharge. The vertical axis is again $[0.99E_{\text{out}}, 1.01E_{\text{out}}]$.

4.3. Convergence to a transcritical steady state with shock wave

The parameters $Q_{\text{in}}, h_{\text{out}}$ used as boundary conditions in the previous numerical example were chosen in a way that the two boundaries are connected by a smooth equilibrium state. A different outward water's depth at the right boundary creates a flow with a stationary shock wave. The flow jumps in a location where the Rankine-Hugoniot conditions are satisfied so as to match the right boundary condition. The details of this numerical experiment are as follows. The topography is given by

$$B(x) = \max\left(\frac{1}{2}\left(1 + \cos\left(\frac{\pi(x-0.5)}{0.4}\right)\right), 0\right), 0 \le x \le 1. \tag{47}$$

The geometry is

$$\sigma(x,z) = \begin{cases} \frac{1}{2} + \left(\frac{1}{2} - (\cos(\pi(x-0.7)/0.2) + 1)/8\right)\sqrt{z} & \text{if} \quad x \in [0.5, 0.9], \\ \frac{1+\sqrt{z}}{2} & \text{if} \quad x \in [0,1] \setminus [0.5, 0.9]. \end{cases} \tag{48}$$

The corresponding discharge and outflow water's depth are $Q_{\text{in}} = 2.5561$ and $h_{\text{out}} = 1.9968$, respectively. Similar to the previous case, at the left boundary we impose Q_{in} and extrapolate h; and at the right boundary we extrapolate Q and either impose h_{out} at inflow

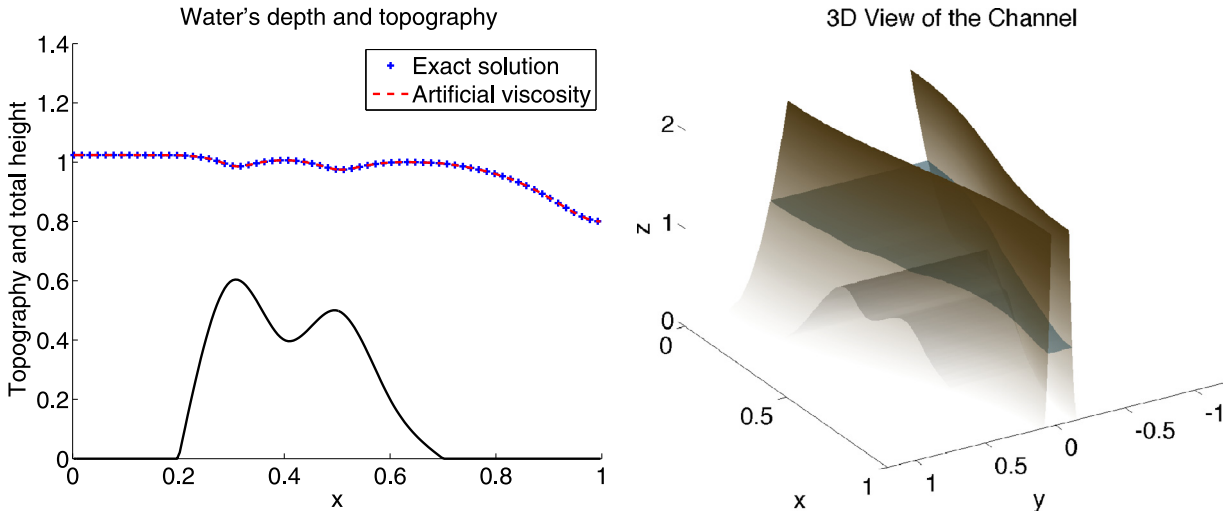

Fig. 3. Convergence to a steady state. Left: 2D view shows the numerical solution obtained using the proposed scheme (dashed red line) and the exact solution(blue "+" signs). The topography is in solid black. Right: 3D view with the walls in "camel" color, topography in grey and water's depth in light blue. (For interpretation of the references to colour in this figure legend, the reader is referred to the web version of this article.)

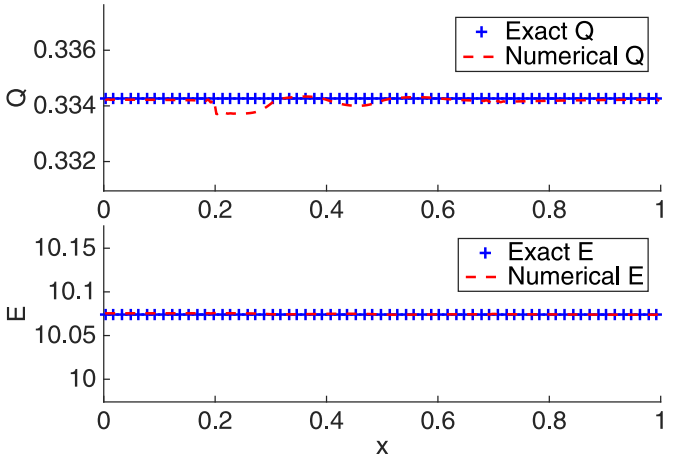

Fig. 4. Convergence to a steady state. Top: Final discharge (dashed red line) and exact discharge Q_{in} (blue "+" signs). Bottom: Energy of the solution (dashed red line) and exact value for the steady state E_{out} (blue "+" signs). (For interpretation of the references to colour in this figure legend, the reader is referred to the web version of this article.)

$(u - c < 0)$ or extrapolate h at outflow $(u - c > 0)$. The flow is discontinuous and transcritical. The flow is subcritical for $0 \le x \le 0.53$, supercritical for $0.53 \le x \le 0.75$ and it jumps back to the subcritical regions at $0.75 \le x \le 1$.

Fig. 5 (left) compares the exact solution (blue solid line) and the numerical approximation (red dashed line). The artificial viscosity is strong enough to keep the oscillations near shock waves under control and it is very small away from discontinuities. Away from the shock wave, the difference between the numerical and exact solutions is not distinguishable. However, near the jump discontinuity we can observe differences that are even more clear when we compare exact and numerical discharge and energy. This is explained below in Fig. 6, and it is due to the viscosity needed near shock waves. However, this is not particular of the artificial viscosity technique, and similar numerical errors are aso observed when nonlinear limiters are implemented. The right panel shows the 3D view. One can see how the flow accelerates as it passes through the top of the topography and channel trough. The flow eventually jumps to match the right boundary conditions, where the channels is wider again.

Fig. 6 exhibits more details of the numerical results (red "+" signs). For comparison, we also include a reference solution using a central-upwind scheme with nonlinear limiters as developed in Balbás and Hernandez-Duenas (2014) (blue dashed line), and the exact solution (black solid line). The left panel has the discharge, which must be constant throughout the domain. The numerical approximation computes the correct value very accurately, except near the shock wave. The piecewise constant exact energy (solid black line) is shown in the right panel, changing across shock waves. Again, the energy of the numerical solution is correctly computed away from the shock wave (red line), and presents errors near the discontinuity. We must say, however, that this is not particular of the artificial viscosity technique. The dashed blue lines show the approximations computed with a central-upwind scheme that uses nonlinear limiters, and it also presents errors near the discontinuity. Similar errors are also observed in Balbás and Karni (2009) (see Figure 11). A more quantitative analysis of the accuracy is the relative error given by (43), which considers the L^2 norm. Since the local error is significant only very close to the shock wave, we believe the L^2 norm is an appropriate measure for the error. In this simulation, the relative error for the discharge and energy are 8.9×10^{-3} and 6.4×10^{-3} respectively.

4.4. Dam-break problem

So far we have tested the well-balance property, and the accuracy of the scheme near shock waves by controlling the oscillations with the artificial viscosity. In this test, we verify numerically that our scheme enjoys the positivity-preserving property. The geometry is again a spline of degree three with nodes (0.1, 1), (0.2, 1), (0.4, 0.5), (0.6, 0.5), (0.8, 0), (1, 0). The geometry is given by

$$\sigma(x,z) = \frac{1}{2} + B(x)(z - B(x)), B(x) \le z \le 2, \tag{49}$$

which describes a channel with a topography with two decreasing bumps and walls with decreasing width from left to right. The initial conditions are

$$u = 0, w = \begin{cases} 1.2 & \text{if } x \le 0.7 \\ B(x) + 10^{-5} & \text{otherwise} \end{cases}, \tag{50}$$

which represent a dam break at $x = 0.3$. The dry region is represented by small values of the water's depth. Here we use a threshold of $h = 10^{-5}$ due to the loss of hyperbolicity when the

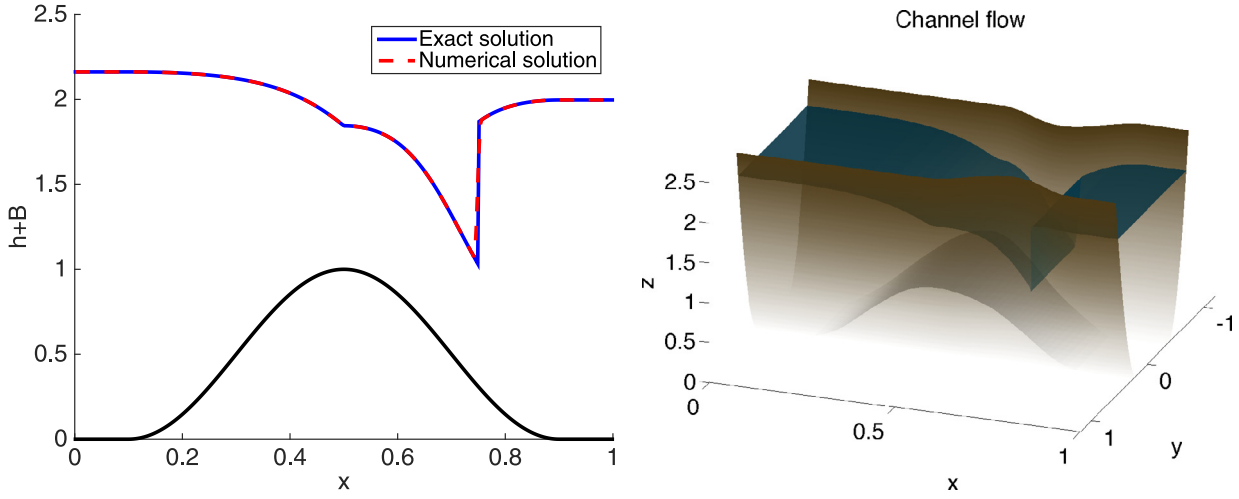

Fig. 5. Convergence to a steady state. Left: 2D view of the numerical solution obtained using the proposed scheme (dashed red line) and the exact solution (solid blue line). The topography is in solid black. Right: 3D-view of the channels showing the topography in grey, walls in "camel" color and water's surface in light blue. (For interpretation of the references to colour in this figure legend, the reader is referred to the web version of this article.)

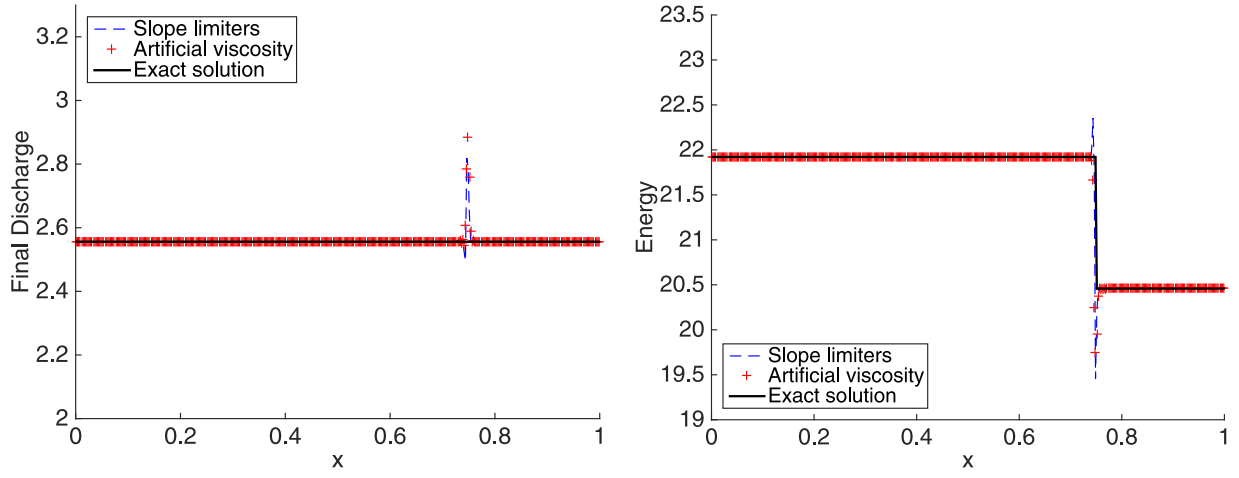

Fig. 6. Convergence to a steady state. The discharge (left) and energy (right) are shown. Black solid line: Exact solution. Dashed blue line: Central-upwind scheme with nonlinear limiters. Red "+" signs: Numerical solution. (For interpretation of the references to colour in this figure legend, the reader is referred to the web version of this article.)

water's depth is zero, and to the positivity-preserving property. A similar threshold is used in the correction (26) and (27). Finally, the boundary conditions here are as follows. The fifth order reconstruction of the solution points $\mathbf{v}(1{:}\ N,\ 1{:}\ 2)$, where N is the number of grid points requires 5 ghost cells in each direction $\mathbf{v}(-4:0, 1:2), \mathbf{v}(N+1:N+5, 1:2)$. At the left boundary, we impose reflecting boundary conditions. That is, we extrapolate A, $A(-1:4) = A(1)$ and the velocity of the ghost cells change sign with their reflective cells $u(j) = -u(1-j), j = -4:0$. At the right boundary, we extrapolate u and either impose $h_{\text{out}} = 10^{-5}$ at outflow ($u - c > 0$) or extrapolate h at inflow ($u - c < 0$).

Fig. 7 shows the evolution of the flow in a dam-break problem at times $t = 0.01, 0.1, 0.5, 5$ with a resolution of $\Delta x = 1/200$ (dashed red lines). Here we have used an artificial viscosity coefficient of $C = 50$. For comparison, we have included a reference solution using the central-upwind scheme with nonlinear limiters developed in Balbás and Hernandez-Duenas (2014). We observe a drainage towards the right, where interactions between wet and dry states occur at all times. The positivity-preserving property allows us to consider simulations of dam breaks, flooding and any type of problems involving wet and dry states. No oscillations are observed despite interactions between wet and dry states or shock waves formed. The final time $t = 5$ is long enough to drain all the water through the right boundary, except for the trapped fluid in both bumps. The total height's relative error according to (43) is computed at $t = 0.5$, before the drainage is completed, giving a value of 1.5×10^{-3}. The CPU time is 800.1 s. The time step varies from 1.19×10^{-4} to 9.96×10^{-4} according to (34) with $\text{CFL}_\epsilon = 0.45$.

Fig. 8 shows a 3D view of the channel at times $t = 0.01$ (top left), $t = 0.1$ (top right), $t = 0.5$ (bottom left), and $t = 5$ (bottom right). The top left panel exhibits the beginning of the dam break. The water starts moving to the right. As it evolves in time, it faces a topography with decreasing bumps and walls that narrow down. The dam is almost dry at $t = 5$, except at the two places where the water was trapped, as shown in the bottom right panel. The proposed numerical scheme guaranties the positivity of the computed values of the water depth in each point of the part of the domain which is almost dry at all times.

4.5. Laboratory and numerical experiments: Dam break over wet bed

Laboratory experiments of dam breaks have been conducted in converging/diverging channels. See for instance, Chapter 5 of the

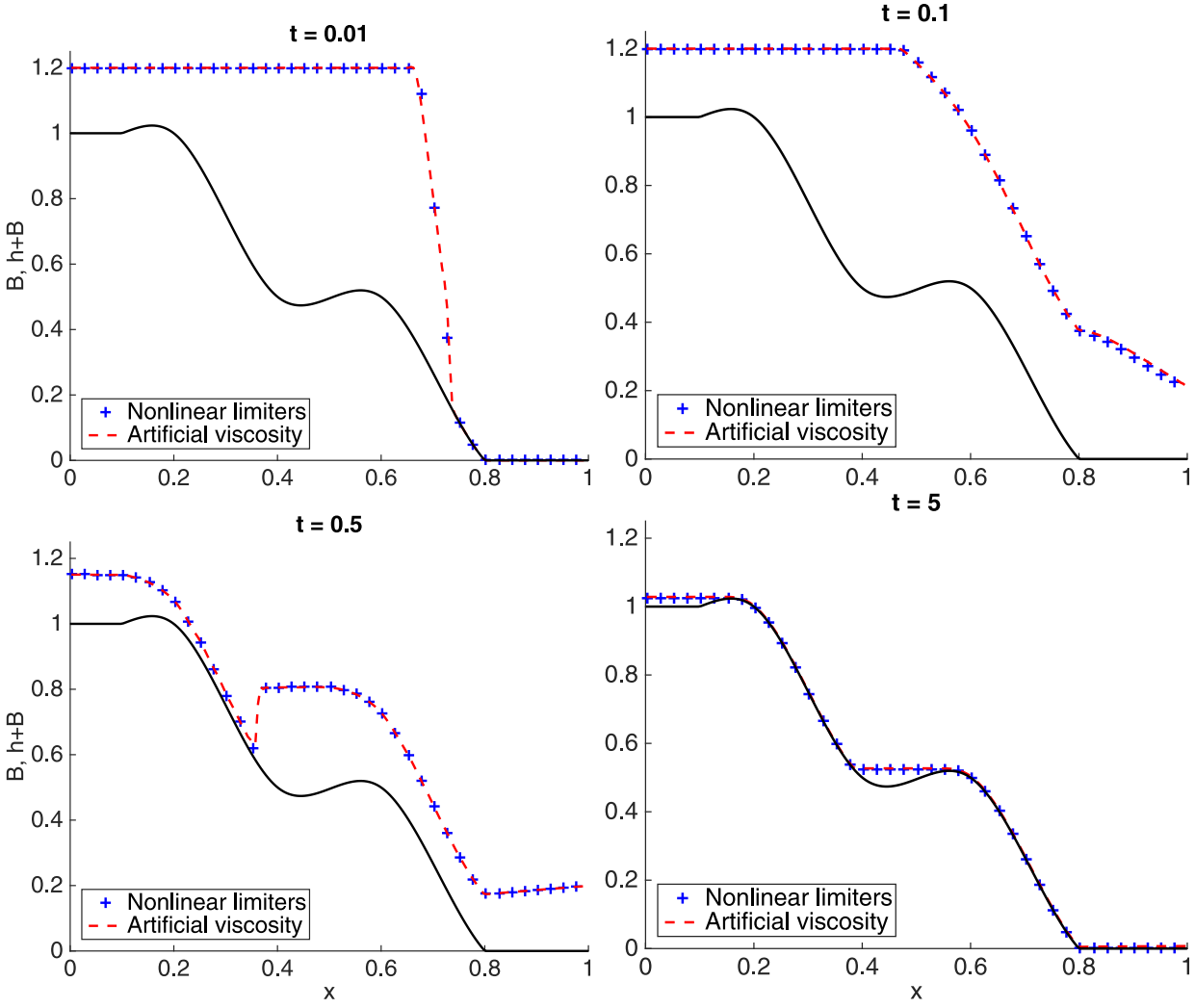

Fig. 7. Dam-break problem. Topography (solid black line) and total height (w) at time $t = 0.01$ (top left), $t = 0.1$ (top right), $t = 0.5$ (bottom left), and $t = 5$ (bottom right). Blue "+" signs: central upwind scheme with slope limiters. Dashed red line: Current scheme. (For interpretation of the references to colour in this figure legend, the reader is referred to the web version of this article.)

book (Khan and Lai, 2014) for a list of experiments in channels with different bed slopes and different wet and dry conditions. We note that in the numerical modeling of those experiments, a friction term has been added to the momentum equation, and the source term now reads

$$\mathbf{S} = \begin{pmatrix} 0 \\ I - gh\sigma_B B' - gAS_f \end{pmatrix}, S_f = \frac{n^2 Q|Q|}{R^{4/3}A^2}, \tag{51}$$

where S_f is the friction slope, n is the Manning roughness coefficient, and R is the hydraulic radius (ratio between the wet area and the wetted perimeter). In the case of rectangular channels with width σ, the hydraulic radius is $R = \sigma h/(\sigma + 2h)$. We note that the friction slope vanishes in steady state at rest, which consequently does not affect the well-balance property. On the other hand, since it appears in the momentum equation, it does not affect the positivity-preserving property either.

The experiments in Khan and Lai (2014) Section 5.3.4 were taken from Bellos et al. (1992). The channel has vertical walls and width variations along the x-axis, approximately given by the graph in the top panel of Fig. 9. The channel's length is 21.2 m, and its width is 1.4 m from 0 to 5 m, 16.8 to 21.2 m. The minimum width is 0.6 m at $x_m = 8.5$ m. The topography in this experiment is flat $B = 0$.

The dam-break problem, taken from Bellos et al. (1992), considers a channel that is initially wet everywhere. Two depths are separated by a gate. Measurements at five different locations and different times are available. The initial conditions are given by

$$u(x, t = 0) = 0, w(x, t = 0) = \begin{cases} 0.3 \text{ m} & \text{if} \quad x < x_m = 8.5 \text{ m}, \\ 0.101 \text{ m} & \text{otherwise}. \end{cases} \tag{52}$$

The gate is assumed to be instantaneously removed. The left boundary is a solid wall. That is, we assume zero Dirichlet boundary conditions for the velocity, with zero Neumann boundary conditions for the height. In reality, a weir is installed at the right boundary. In the numerical simulations, we extrapolate the water's height at outflow and impose $h_{\text{out}} = 0.101$ at inflow. Following (Khan and Lai, 2014), we impose a discharge given by Bazin's formula

$$Q = \frac{2}{3} C_d b (2g)^{2/3} (h + B - 0.101)^{1.5}, \tag{53}$$

where $C_d = 0.62$ is the discharge coefficient, $b = 1.4$ m is the length of the weir, and the topography $B = 0$ is flat in our simulations. We have also applied the friction term as in (51), with Manning coefficient $n = 1.8 \times 10^{-2}$ s m$^{-1/3}$.

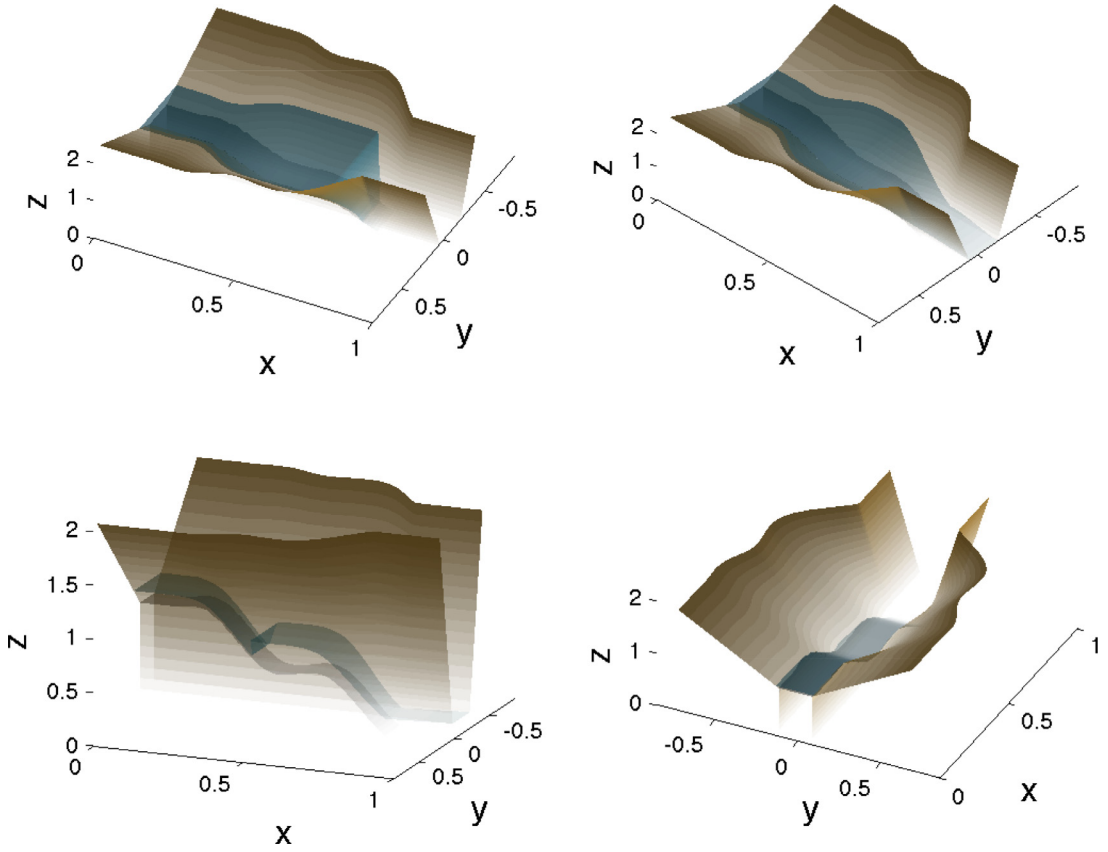

Fig. 8. Dam-break problem and its 3D view. Topography (grey), walls ("camel" color) and total height (blue) are shown at times $t = 0.01$ (top left), $t = 0.1$ (top right), $t = 0.5$ (bottom left), and $t = 5$ (bottom right). Different views of the channel are used. (For interpretation of the references to colour in this figure legend, the reader is referred to the web version of this article.)

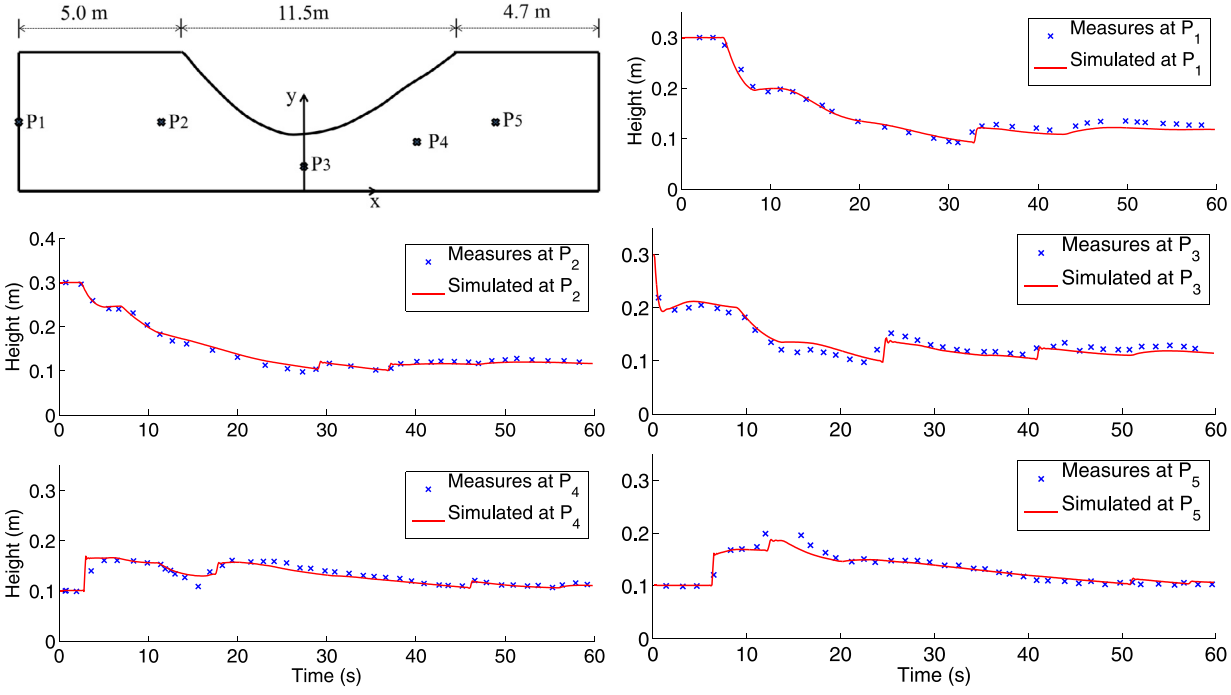

Fig. 9. Comparison of laboratory and numerical simulations in a dam break over wet bed. Top left: Aerial view of the channel with the location of the five points of measurements: $P_{1,2,3,4,5} = 0, 4.5, 8.5, 13.5, 18.5$ m. The rest of the panel from left to right, top to bottom shows the measured and numerically approximated water's height. The measured values are shown by blue crosses, and the numerical approximations are given by the red solid lines. (For interpretation of the references to colour in this figure legend, the reader is referred to the web version of this article.)

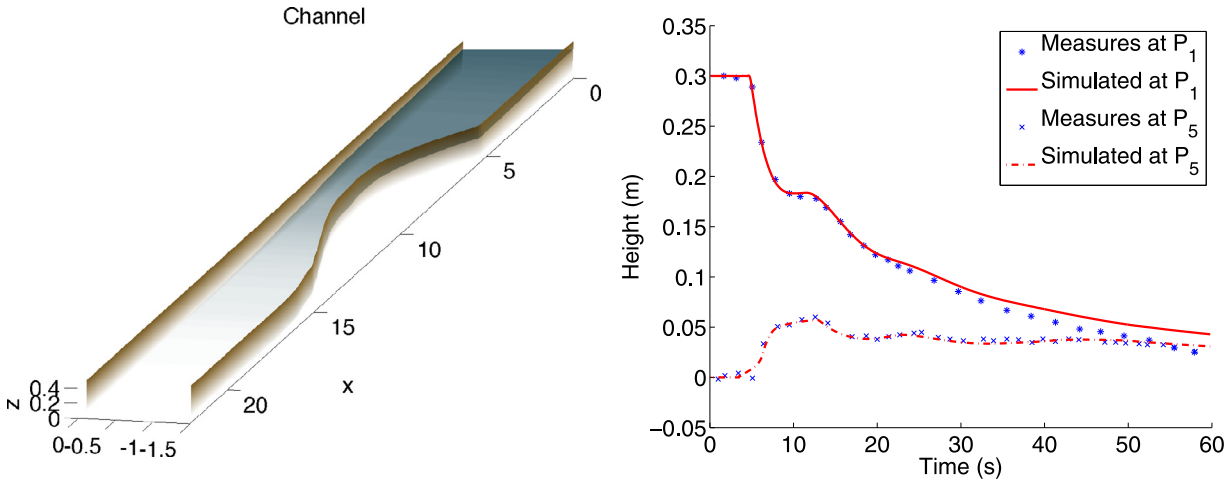

Fig. 10. Comparison of experimental data and numerical simulations. Left: 3D view of the channel and the solution at time $t = 5$ s for the dam-break problem in Eq. (54). Right: comparison between experimental data and the numerical approximation obtained by the present schemes of the water's height at two particular locations in x, *versus* time. The left point is located at the left boundary $P_1 = 0$, and the right point is located at $P_5 = 18.5$m.

Fig. 9 shows the comparison between the measured values at five points $P_{1,2,3,4,5} = 0, 4.5, 8.5, 13.5, 18.5$ m and the numerical approximations, with respect to time. We observe good agreement in all measurements, and the differences might be due to unavailable configuration of the weir at the downstream, as it was pointed out in Khan and Lai (2014). The boundary conditions might play an important role. The downstream front reaches the right boundary after 8.5 s, approximately. After that point, our choice of the boundary condition at the right can influence and affect the predictions. The time step according to the CFL condition (34) varies from 1.9×10^{-2} s to 4.3×10^{-3} s in a resolution of $\Delta x = 21.2$ m/200, compared to a time step of 3×10^{-3} s and 2×10^{-4} s, and a resolution of 0.1 m used in Bellos et al. (1992). The CPU time for this simulation was 199 s.

4.6. Laboratory and numerical experiment: Dam break over dry bed

The same channel from Section 4.5 is considered. However, we only have experimental information available at P_1 and P_5. The flow is initially given by

$$u(x, t = 0) = 0, w(x, t = 0) = \begin{cases} 0.3\,\text{m} & \text{if} \quad x < x_m = 8.5\ \text{m}, \\ h_{\text{out}} = 10^{-5}\text{m} & \text{otherwise}, \end{cases} \tag{54}$$

which corresponds to a flow initially at rest, where the downstream part of the channel is dry (a threshold value has been used). We have used zero Dirichlet left boundary conditions in the velocity and Neumann left boundary conditions for the height. The right boundary extrapolates the data at outflow, and imposes h_{out} at inflow. The Manning roughness coefficient is set to $n = 8.4 \times 10^{-3}$ s m$^{-1/3}$. Once the dam breaks, the flow evolves as illustrated in the left panel of Fig. 10 at $t = 5$ s. The resolution here is $\Delta x = 21.2$ m/200.

In the experimental data in Bellos et al. (1992), Khan and Lai (2014), the height was measured in time at two particular locations. One at the left boundary $P_1 = 0$, and the other one near the right boundary $P_5 = 18.5$ m. The aerial view of the channel is shown in the top left panel of Fig. 9. The right panel in Fig. 10 compares the real and numerical values. We observe a good agreement, specially at the location P_5 near the right boundary, for the entire simulation. The numerical approximation at P_1 is accurate for the first part of the simulation, and overestimates it for the second half. Boundary conditions and the adjustment of the Manning coefficient might affect the predictions. In the current simulations, the CPU time was 219.9 s, and the time step varies from 1.0×10^{-2} to 4.1×10^{-2} s.

5. Discussion of the main results

In this section, we discuss the main contributions of the paper and summarize the results. We considered a shallow water model in channels with irregular geometry and variable topography which is an intermediate case between the one- and two- dimensional models. The system is obtained by integrating the Euler equations in each cross section, under reasonable assumptions stating that the velocity along the channel axis is dominating and that the flow has relatively uniform distribution over each channel's cross section. This model has many practical hydraulic applications. The one-dimensional nature of the system offers simulations that are computationally cheap when a robust and efficient numerical method can be developed.

The shallow water flows in channels is proposed as a one-dimensional system with two-dimensional aspects, since the channel's width varies vertically. The properties of the model were discussed. The model consists of a system of hyperbolic balance laws, and it looses hyperbolicity in dry states. As other balance laws, different types of numerical schemes can be implemented to solve the system. Each class of numerical algorithms may offer specific advantages. Previous works that use nonlinear limiters to maintain the non-oscillatory behavior near jump discontinuities were discussed and the references provided. It is well documented that extensions to higher order approximations are computationally expensive, and an alternative is the goal of this paper. A novel high-order non-oscillatory, free of Riemann-solver method with artificial viscosity is developed for shallow-water systems in channels with arbitrary geometry and variable bed topography. The artificial viscosity is used as an alternative to computationally expensive techniques such as nonlinear limiters. A high-order reconstruction of interface cell values supplemented with the adaptive artificial viscosity approach are implemented. This is done in combination with the topography source term discretization and the geometry of the channel to simultaneously satisfy three desirable properties: conservation (by construction), well-balance, and positivity-preserving. The well-balance property was obtained with a suitable discretization of the source terms. We also showed that a slightly more restrictive time step condition than that given by CFL

guarantees the positivity of the water's depth as we evolve the numerical approximation in time. This makes the development of robust and efficient numerical approximations methods more challenging.

As stated above, we develop a central-upwind scheme which respects two main proprieties. First, the well-balanced property of the proposed scheme is ensured using suitable discretization techniques by properly taking into account the effects induced by the geometry of the channel and the variable topography. The second property is positivity preserving: the proposed method guarantees the positivity of the computed values of the water's depth in each point of the domain at all times. Several numerical examples are performed to exhibit the merits of the proposed method. A first numerical test dealt with perturbations of the water surface elevation of a "lake at rest" over variable topography and geometry. The numerical results showed that the solution is free of numerical oscillations and the scheme is well-balanced, inducing stability and improving the accuracy of near steady-state flows. The efficiency of the method was analyzed in this numerical example, compared to a Roe-type upwind scheme. We claimed that our numerical algorithm is accurate for near steady-state flows and two tests were carried out in that direction. A smooth subcritical steady state with constant discharge and energy is used as a reference solution. Under appropriate boundary conditions, the flow converges to the prescribed steady state. The numerical results showed that the computed solutions are oscillation-free and accurately resolved. On the other hand, an alternative boundary condition gave us a flow evolution that converged to a transcritical steady state with a shock wave. The numerical approximation was very accurate, except near the jump discontinuity. It was explained that those errors are very localized and are not attached to the proposed artificial viscosity approach. References were provided where similar errors were reported. In addition to the numerical tests using steady state solutions, the proposed method was tested using solutions with rapidly varying flows. We considered two types of numerical tests for the simulation of a dam break over variable bottom topography. First, the results obtained using the prosed method were compared to those obtained using central-upwind scheme with nonlinear limiters. The second numerical test is performed using laboratory experiments of dam breaks in converging/diverging channels. A friction source term was incorporated to the model. Accurate results are obtained for both the case of dam break over dry bed and the case of dam break over wet bed. These numerical tests confirm stability, positivity-preserving properties and high resolution of the proposed scheme.

6. Conclusions

A novel high-resolution, semi-discrete central-upwind scheme is proposed for shallow-water flows in channels. The high resolution techniques are used with the artificial viscosity instead of nonlinear limiters which are computationally expensive. A new technique for channels is proposed for the correction of the water surface elevation at the interfaces of computational cells which insure the positivity-preserving property of the proposed method. The well-balanced property of the proposed central-upwind scheme is ensured using a special discretization for the cell averages of the source terms in which we take into account the impact of the complex geometry of the channel. The performances of the proposed scheme are tested on a number of numerical examples and the desirable properties such as well-balance, stability, positivity-preserving and accuracy were discussed. We showed that a slightly more restrictive time step condition than that given by CFL guarantees the positivity of the water's depth as we evolve the numerical approximation in time. The proposed central-upwind method presents the advantage of using artificial viscosity with high-order non-limited reconstructions. This scheme can be applied to shallow flows in channels with variable topography and complex geometry.

Acknowledgements

This research was supported in part by grant UNAM-DGAPA-PAPIIT IA103015. The authors thank the three anonymous reviewers for their valuable comments and suggestions to improve the quality of the paper.

References

Armi, L., 1986. The hydraulics of two flowing layers with different densities. J. Fluid Mech. 163, 27–58. http://dx.doi.org/10.1017/S0022112086002197.

Armi, L., Farmer, D.M., 1986. Maximal two-layer exchange through a contraction with barotropic net flow. J. Fluid Mech. 186, 27–51.

Audusse, E., Bouchut, F., Bristeau, M.-O., Klein, R., Perthame, B., 2004. A fast and stable well-balanced scheme with hydrostatic reconstruction for shallow water flows. SIAM J. Sci. Comput. 25 (6), 2050–2065(electronic). http://dx.doi.org/10.1137/S1064827503431090.

Balbás, J., Hernandez-Duenas, G., 2014. A positivity preserving central scheme for shallow water flows in channels with wet-dry states. ESAIM Math. Model. Numer. Anal. 48 (3), 665–696. http://dx.doi.org/10.1051/m2an/2013106.

Balbás, J., Karni, S., 2009. A central scheme for shallow water flows along channels with irregular geometry. M2AN Math. Model. Numer. Anal. 43 (2), 333–351. http://dx.doi.org/10.1051/m2an:2008050.

Beljadid, A., Mohammadian, A., Kurganov, A., 2016. Well-balanced positivity preserving cell-vertex central-upwind scheme for shallow water flows. Comput. Fluids 136, 193–206.

Bellos, C.V., Soulis, V., Sakkas, J.G., 1992. Experimental investigation of two-dimensional dam-break induced flows. J. Hydraul. Res. 30 (1), 47–63.

Bouchut, F., 2004. Nonlinear stability of finite volume methods for hyperbolic conservation laws and well-balanced schemes for sources. Frontiers in Mathematics. Birkhäuser Verlag, Basel.

Castro, M., Macías, J., Parés, C., 2001. A *Q*-scheme for a class of systems of coupled conservation laws with source term. Application to a two-layer 1-D shallow water system. M2AN Math. Model. Numer. Anal. 35 (1), 107–127. http://dx.doi.org/10.1051/m2an:2001108.

Castro, M.J., García-Rodríguez, J.A., González-Vida, J.M., Macías, J., Parés, C., Vázquez-Cendón, M.E., 2004. Numerical simulation of two-layer shallow water flows through channels with irregular geometry. J. Comput. Phys. 195 (1), 202–235. http://dx.doi.org/10.1016/j.jcp.2003.08.035.

Chen, Y., Kurganov, A., Lei, M., Liu, Y., 2013. An adaptive artificial viscosity method for the Saint-Venant system. In: Recent Developments in the Numerics of Nonlinear Hyperbolic Conservation Laws. In: Notes Numer. Fluid Mech. Multidiscip. Des., vol. 120. Springer, Heidelberg, pp. 125–141. http://dx.doi.org/10.1007/978-3-642-33221-0_8.

Črnjarić-Žic, N., Vuković, S., Sopta, L., 2004. Balanced finite volume WENO and central WENO schemes for the shallow water and the open-channel flow equations. J. Comput. Phys. 200 (2), 512–548. http://dx.doi.org/10.1016/j.jcp.2004.04.012.

Farmer, D.M, Armi, L., 1986. Maximal two-layer exchange over a sill and through the combination of a sill and contraction with barotropic flow. J. Fluid Mech. 164, 53–76.

Garcia-Navarro, P., Vazquez-Cendon, M.E., 2000. On numerical treatment of the source terms in the shallow water equations. Comput. Fluids 29 (8), 951–979.

George, D.L., 2008. Augmented Riemann solvers for the shallow water equations over variable topography with steady states and inundation. J. Comput. Phys. 227 (6), 3089–3113. http://dx.doi.org/10.1016/j.jcp.2007.10.027.

Gosse, L., Leroux, A.-Y., 1996. Un schéma-équilibre adapté aux lois de conservation scalaires non-homogènes. C. R. Acad. Sci. Paris Sér. I Math. 323 (5), 543–546.

Gottlieb, S., Shu, C.-W., Tadmor, E., 2001. Strong stability-preserving high-order time discretization methods. SIAM Rev. 43 (1), 89–112(electronic). http://dx.doi.org/10.1137/S003614450036757X.

Greenberg, J.M., Leroux, A.Y., 1996. A well-balanced scheme for the numerical processing of source terms in hyperbolic equations. SIAM J. Numer. Anal. 33 (1), 1–16. http://dx.doi.org/10.1137/0733001.

Guermond, J.-L., Pasquetti, R., Popov, B., 2011. Entropy viscosity method for nonlinear conservation laws. J. Comput. Phys. 230 (11), 4248–4267. http://dx.doi.org/10.1016/j.jcp.2010.11.043.

Harten, A., 1983. High resolution schemes for hyperbolic conservation laws. J. Comput. Phys. 49, 357–393.

Hernández-Dueñas, G., Karni, S., 2011. Shallow water flows in channels. J. Sci. Comput. 48 (1–3), 190–208. http://dx.doi.org/10.1007/s10915-010-9430-x.

Jin, S., 2001. A steady-state capturing method for hyperbolic systems with geometrical source terms. M2AN Math. Model. Numer. Anal. 35 (4), 631–645. http://dx.doi.org/10.1051/m2an:2001130.

Khan, A.A., Lai, W., 2014. Modeling Shallow Water Flows Using the Discontinuous Galerkin Method. CRC Press.

Kurganov, A., Levy, D., 2002. Central-upwind schemes for the Saint-Venant system. M2AN Math. Model. Numer. Anal. 36 (3), 397–425. http://dx.doi.org/10.1051/m2an:2002019.

Kurganov, A., Lin, C.-T., 2007. On the reduction of numerical dissipation in central-upwind schemes. Commun. Comput. Phys. 2 (1), 141–163.
Kurganov, A., Liu, Y., 2012. New adaptive artificial viscosity method for hyperbolic systems of conservation laws. J. Comput. Phys. 231 (24), 8114–8132. http://dx.doi.org/10.1016/j.jcp.2012.07.040.
Kurganov, A., Noelle, S., Petrova, G., 2001. Semidiscrete central-upwind schemes for hyperbolic conservation laws and Hamilton-Jacobi equations. SIAM J. Sci. Comput. 23 (3), 707–740(electronic). http://dx.doi.org/10.1137/S1064827500373413.
Kurganov, A., Petrova, G., 2007. A second-order well-balanced positivity preserving central-upwind scheme for the Saint-Venant system. Commun. Math. Sci. 5 (1), 133–160.
Kurganov, A., Petrova, G., 2009. Central-upwind schemes for two-layer shallow water equations. SIAM J. Sci. Comput. 31 (3), 1742–1773. http://dx.doi.org/10.1137/080719091.
Kurganov, A., Tadmor, E., 2000. New high-resolution central schemes for nonlinear conservation laws and convection-diffusion equations. J. Comput. Phys. 160 (1), 241–282.
Kurganov, A., Tadmor, E., 2002. Solution of two-dimensional Riemann problems for gas dynamics without Riemann problem solvers. Numer. Methods Partial Differential Eqs. 18 (5), 584–608. http://dx.doi.org/10.1002/num.10025.
LeVeque, R.J., 1998. Balancing source terms and flux gradients in high-resolution Godunov methods: the quasi-steady wave-propagation algorithm. J. Comput. Phys. 146 (1), 346–365. http://dx.doi.org/10.1006/jcph.1998.6058.
LeVeque, R.J., George, D.L., Berger, M.J., 2011. Tsunami modelling with adaptively refined finite volume methods. Acta Numer. 20, 211–289. http://dx.doi.org/10.1017/S0962492911000043.
Noelle, S., Pankratz, N., Puppo, G., Natvig, J.R., 2006. Well-balanced finite volume schemes of arbitrary order of accuracy for shallow water flows. J. Comput. Phys. 213 (2), 474–499. http://dx.doi.org/10.1016/j.jcp.2005.08.019.
Noelle, S., Xing, Y., Shu, C.-W., 2007. High-order well-balanced finite volume WENO schemes for shallow water equation with moving water. J. Comput. Phys. 226 (1), 29–58. http://dx.doi.org/10.1016/j.jcp.2007.03.031.
Perthame, B., Simeoni, C., 2001. A kinetic scheme for the Saint-Venant system with a source term. Calcolo 38 (4), 201–231. http://dx.doi.org/10.1007/s10092-001-8181-3.
Roe, P.L., 1987. Upwind differencing schemes for hyperbolic conservation laws with source terms. In: Nonlinear Hyperbolic Problems (St. Etienne, 1986). In: Lecture Notes in Math., vol. 1270. Springer, Berlin, pp. 41–51. http://dx.doi.org/10.1007/BFb0078316.
Russo, G., 2001. Central schemes for balance laws. In: Hyperbolic Problems: Theory, Numerics, Applications, Vol. I, II (Magdeburg, 2000). In: Internat. Ser. Numer. Math., 140, vol. 141. Birkhäuser, Basel, pp. 821–829.
Russo, G., 2005. Central schemes for conservation laws with application to shallow water equations. In: Trends and Applications of Mathematics to Mechanics. Springer, pp. 225–246.
Shu, C.-W., 2009. High order weighted essentially nonoscillatory schemes for convection dominated problems. SIAM Rev. 51 (1), 82–126. http://dx.doi.org/10.1137/070679065.
Shu, C.-W., Osher, S., 1989. Efficient implementation of essentially nonoscillatory shock-capturing schemes. II. J. Comput. Phys. 83 (1), 32–78. http://dx.doi.org/10.1016/0021-9991(89)90222-2.
Sweby, P.K., 1984. High resolution schemes using flux limiters for hyperbolic conservation laws. SIAM J. Numer. Anal. 21 (5), 995–1011. http://dx.doi.org/10.1137/0721062.
Szymkiewicz, R., 2010. Numerical Modeling in Open Channel Hydraulics, 83. Springer Science & Business Media.
Vázquez-Cendón, M.E., 1999. Improved treatment of source terms in upwind schemes for the shallow water equations in channels with irregular geometry. J. Comput. Phys. 148 (2), 497–526. http://dx.doi.org/10.1006/jcph.1998.6127.
Vuković, S., Sopta, L., 2003. High-order ENO and WENO schemes with flux gradient and source term balancing. In: Applied Mathematics and Scientific Computing (Dubrovnik, 2001). Kluwer/Plenum, New York, pp. 333–346.